RSC Advances

Check for updates

Enhancing the antioxidant potential of a coumarin derivative *via* nickel complexation: synthesis, spectral insights, DFT analysis, and molecular docking

Hayet. Belbah,[a] Karima. Belguidoum,[a] Zeyneb. Ourdjini,[b] Fatima. Zahra Hamamdia,[a] Fatiha. Madi,[c] Leila. Nouar,[c] Mouna. Nacef, [ID] *[d] Mohammed Hadj Mortada Belhachemi,[e] Habiba Amira-Guebailia[a] and Abdelkader Chouaih[e]

Daphnetin is a naturally occurring coumarin. Despite its numerous positive biological effects, progress in its clinical trial use has been minimal due to its poor water solubility and limited oral bioavailability. This study focuses on the development of a novel and highly stable daphnetin–nickel complex (Ni–DAPH). We present a comprehensive investigation combining experimental and computational approaches to explore the synthesis, characterization, properties, reactivity, and biological activity of the Ni–DAPH complex. The computational studies, based on DFT, included geometry optimization HOMO and LUMO orbitals, UV-visible spectra, infrared (IR) and nuclear magnetic resonance (NMR) spectra, molecular electrostatic potential (MEP), non-covalent interaction (NCI) analysis, quantum theory of atoms in molecules (QTAIM), nonlinear optical (NLO) properties, and antioxidant activity. The molecular electrostatic potential (MEP) analysis identified nucleophilic and electrophilic sites within the complex, while the infrared spectra pinpointed the carbonyl group of the benzopyrone ring as the primary site of complexation. NMR spectroscopy revealed significant proton involvement in charge transfer between the ligand and the nickel center. Natural bond orbital (NBO) analysis indicated nearly equivalent bond angles, suggesting a symmetric geometry. QTAIM analysis confirmed the presence of ionic bonding with a partial covalent character, enhancing the stability of the complex. The ordering of the nickel 3d orbitals is characteristic of a distorted square-planar geometry. The hydrogen atom transfer (HAT) mechanism demonstrated that the Ni–DAPH complex exhibits significantly enhanced antioxidant activity in comparison to the free daphnetin ligand. This result was confirmed by molecular docking with the cytochrome C peroxidase (CCP) and ascorbate peroxidase (APX) HEME-enzymes, using the 2X08 and 1OAF receptor structures. The *in silico* ADMET study reveals that DAPH complexation improves intestinal absorption and reduces toxicity, enhancing the pharmacological potential of Ni–DAPH.

1 Introduction

The activation of organic compounds by metals, such as nickel, iron, and copper, enables the development of new molecules, resulting in a wide range of applications in fields including reagents for organic synthesis, catalysis, medicine, and biology.[1–6]

In the past two decades, significant research has been devoted to exploring the unique characteristics of organometallic and coordination complexes (*e.g.*, structural diversity, ligand exchange capability, redox and catalytic properties) for medicinal purposes.[2] Complexes formed between naturally derived compounds, such as polyphenols, and metals are particularly intriguing as they enhance the chemical properties of these molecules, resulting in clusters with improved biological properties.[5,7]

Among polyphenols, coumarins are phytochemicals that exhibit diverse biological activities, indicating their ability to interact with various cellular targets. Their structural and physicochemical characteristics render them highly promising

[a]*Laboratory of Applied Chemistry -LCA, University 8 May 1945, BP 401, Guelma 24000, Algeria*

[b]*Department of matter Sciences, Faculty of mathematics, computer and matter Sciences, University 8 May 1945, BP 401, Guelma 24000, Algeria*

[c]*Laboratory of Computational Chemistry and Nanostructure, University 8 May 1945, BP 401, Guelma 24000, Algeria*

[d]*Laboratory of Industrial Analysis and Materials Engineering, University May 8 1945, BP 401, Guelma 24000, Algeria. E-mail: nacef.mouna@univ-guelma.dz; nacef2010@yahoo.fr*

[e]*Laboratory of Technology and Solid Properties (LTPS), Faculty of Sciences and Technology, Abdelhamid Ibn Badis University of Mostaganem, 27000 Mostaganem, Algeria*

compounds in the field of medicinal chemistry and chemical biology.[8] In recent years, both natural and synthetic coumarins have shown considerable potential in the domain of cancer treatment.[9–11]

In addition to their versatile structure for drug design, coumarins serve an important function as fluorescent probes for identifying metals, enzymes, and biomaterials.[12,13]

Daphnetin, or 7,8-dihydroxycoumarin (DAPH) a coumarin found in various plants, including *Daphne gnidium* L., has been noted to have multiple biological activities, such as anti-inflammatory, antioxidant, antimicrobial, anti-cancer, anti-hypoxic, neuroprotective, anti-proliferative, anti-diarrheal, and antiparasitic effects.[14–18]

Despite the wide array of beneficial biological effects associated with daphnetin, there has been limited advancement in its translation to clinical trials. The utilization of daphnetin as a fully-fledged therapeutic agent is hindered by its poor water solubility and low oral bioavailability.[19] Conversely, it has been noted that the addition of a metal ion to coumarin derivatives may enhance the activity of these complexes in comparison to coumarin-based ligands. Balewski and colleagues provided a comprehensive overview of the latest developments in coumarin-metal complexes, highlighting their roles as anti-cancer, antimicrobial, antifungal, and antioxidant agents, in addition to their functions as enzyme mimics and inhibitors.[20]

In the context of this investigation, we aim to enhance the characteristics of daphnetin by introducing a novel approach involving its complexation with a transition metal, specifically nickel. This proposed method not only seeks to augment the inherent properties of daphnetin but also contributes to the advancement of strategies aimed at optimizing its therapeutic potential. Through the intricate interplay between daphnetin and nickel, we endeavor to unlock new avenues for improving its efficacy, bioavailability, and overall suitability for pharmaceutical applications.

The synthesized organometallic complex Ni-DAPH was identified experimentally using UV-visible infrared and NMR spectroscopies. The geometry of the formed complex, as well as its stability and reactivity were investigated through density functional theory (DFT) calculations using the Gaussian 09 software.

The molecular structure, frontier molecular orbital energies, atomic charges, and molecular, electrostatic potential (MEP) of the title complex were studied. Spectral analyses comprising UV-vis, Infrared and NMR spectra were performed. The complex was subjected to analyses using NBO, NCI, QTAIM and NLO to investigate its symmetry, non-covalent interactions, binding and optical characteristics.

Furthermore, we have also investigated the antioxidant activity of both free ligand (daphnetin) and Ni–DAPH complex using the HAT mechanism. Antioxidant activity is a critical property, as compounds with strong antioxidant potential can neutralize reactive oxygen species (ROS) and mitigate oxidative stress, which serves as a crucial element in the advancement of various diseases, including cancer. To confirm this activity, a detailed molecular docking investigation was performed. Finally, ADMET property analysis is an essential step in the early

evaluation of a compound's pharmacological potential. In this study, it was used to predict the bioavailability, toxicity, and distribution profiles of the DAPH molecule and its nickel-based complex (Ni–DAPH). These approaches allow for rapid estimation of a compound's compatibility with oral administration, as well as its behavior in the body.

2 Experimental

2.1 Chemicals and solvents

All solvents and reagents used in this study were of high quality and were used as received without any further purification. The ligand (daphnetin) (Fig. 1) and nickel(II) acetate tetrahydrate (Ni(OAc)$_2$·4H$_2$O) were acquired from Sigma-Aldrich with a purity exceeding 97%.

2.2 Instrumental analysis

2.2.1 Electronic spectra. The electronic absorption spectra of methanolic solutions containing the ligand and the complex were obtained utilizing UV Probe PC software, covering the wavelength range of 1100–190 nm. This analysis was conducted with a PerkinElmer Lambda 25 UV/Vis double beam spectrophotometer, which was fitted with a quartz cell having a path length of 1 cm.

2.2.2 Infrared spectra. The infrared spectra of both the free ligand and the complex were obtained as KBr discs utilizing an Agilent FT-IR spectrometer. The measurements were performed over a range of 4000 to 400 cm^{-1}, comprising 74 scans at a resolution of 4 cm^{-1}.

2.3 Synthesis of Ni–DAPH complex

An amount of 9 mg of nickel(II) acetate tetrahydrate (Ni(OAc)$_2$·4H$_2$O) was accurately weighed and dissolved in a solvent mixture consisting of 5 mL of methanol and 2 mL of distilled water, under continuous stirring to ensure complete dissolution. In a separate beaker, 12.2 mg of the ligand 7,8-dihydroxycoumarin (commonly known as daphnetin) was dissolved in 5 mL of methanol at room temperature. The ligand solution was then added dropwise to the metal salt solution under magnetic stirring to promote homogeneous mixing and allow coordination between the Ni^{2+} ions and the phenolic groups of the ligand.

The resulting mixture was subjected to reflux at a controlled temperature of 40 °C for 20–30 minutes, a mild condition that facilitates complexation while preventing degradation of the ligand or solvent evaporation. During the reflux, the formation of a green precipitate was observed, indicating the successful coordination of Ni^{2+} with the daphnetin ligand. Upon cooling to room temperature, the reaction mixture was centrifuged at
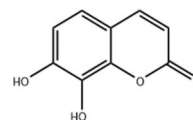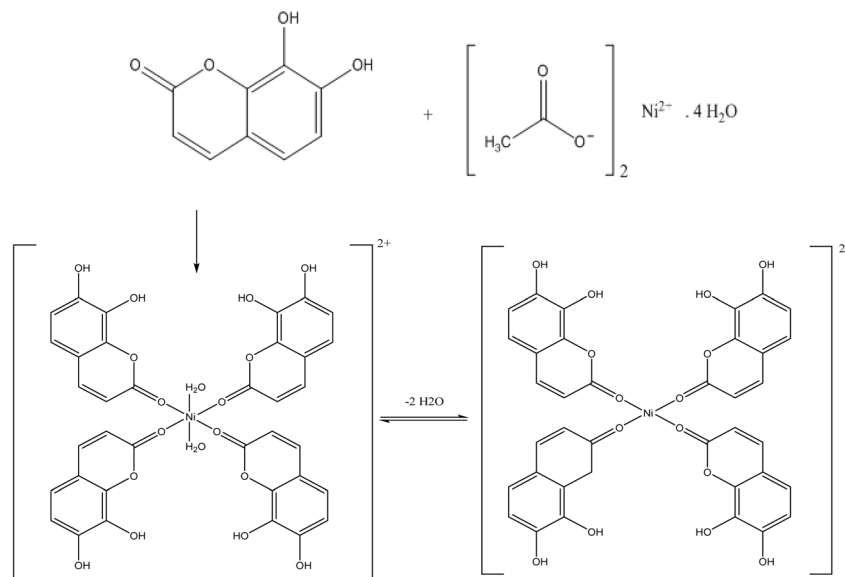

Fig. 1 Chemical structure of daphnetin.

Fig. 2 Suggested structure of Ni–DAPH complex.

4000 rpm for 10 minutes to separate the solid product from the reaction medium. The supernatant was carefully decanted, and the residue was washed with small portions of cold methanol to remove unreacted species and byproducts.[21]

The resulting solid, corresponding to the Ni–DAPH complex, was collected and dried. The final product was obtained as a dark green powder, suggesting the presence of a chelated Ni(II) center (Fig. 2).

3 Computational procedure

All quantum chemical calculations in this study were conducted utilizing the Gaussian 09 software.[22] The ligand optimization was carried out using the B3LYP/6-311++G (d, p) hybrid functional. For the calculations of the Ni–DAPH complex, the B3LYP hybrid functional was combined with the LANL2DZ (Los Alamos National Laboratory 2 double-ξ) basis[23] which is a set of functions used in quantum chemistry calculations to represent the electron orbitals of atoms in a molecule. It is particularly designed for heavy/transition elements, incorporating a larger basis set for the innermost electrons (core) and a smaller set for the outer electrons (valence). This allows for a more efficient description of electron distribution in heavy atoms, balancing computational accuracy and efficiency.

After optimizing the geometries of the DAPH ligand and the Ni–DAPH complex, the study of their antioxidant activity was carried out. Molecular electrostatic potential (MEP) was used to identify the locations of electrophilic and nucleophilic sites using the same parameters. The distribution of electron densities was also determined. The frontier orbitals HOMO and LUMO were identified, and their energies were calculated. Atomic charge calculations were performed, as they play a crucial role in the application of quantum calculations to molecular systems, influencing properties such as dipole moment, polarizability, and electronic structure.[24]

4 Results and discussion

4.1 Characterization of the complex

The synthesized nickel–daphnetin complex was obtained as a crystalline solid with a melting point of 298 °C, indicating good thermal stability and suggesting a pure product. The sharp melting point reflects the defined crystalline nature of the complex.

The elemental composition of the proposed [Ni(Daphnetin)$_4$] complex ($C_{36}H_{24}NiO_{16}$) was calculated as: C, 56.06%; H, 3.14%; O, 33.20%; and Ni, 7.61%. This calculation supports the expected molecular formula of the complex [Ni($C_9H_6O_4$)$_4$].

4.1.1 UV-vis absorption

4.1.1.1 Ligand. 205 nm (^1L_a) a π–π* transition with some intramolecular charge-transfer character due to the electronic effects of the hydroxyl substituents, 265 nm (262.[25]) (a π–π* transition or K band), 330 nm (325.[25]) nm (to a π–π* transition or B band of a substituted aromatic derivative) (Fig. S1).

4.1.1.2 Complex NI–DAPH. 450 nm with higher absorbance in the daphnetin–Nickel complex is likely due to a ligand-to-metal charge transfer (LMCT) transition where electron density shifts from the daphnetin ligand to the nickel center, resulting in a more intense band or π–π* transitions within the ligand moiety, possibly perturbed by coordination with nickel) 750 nm d–d transitions within the Ni(II) center (Fig. S2).

4.1.2 Vibrational spectra analysis.

The IR spectrum (Fig. S3A) indicates the presence of functional groups consistent with a coumarin structure (Table 1).[26] Specifically, A wide band is detected between 3100–3600 cm^{-1}, pertaining to an O–H group involved in hydrogen bonding, either intramolecular (within the daphnetin molecule) or intermolecular (with other daphnetin or solvent molecules). The carbonyl band at 1650 cm^{-1} arises from the conjugation of the carbonyl group featuring double bonds within the aromatic ring. The infrared

Table 1 Vibrational frequencies (cm^{-1}) and tentative band assignments for DAPH and Ni–DAPH complex

Wavenumber $\bar{\upsilon}$ (cm^{-1})			
Ligand	Complex	Assignment	Observation
3100–3600	3100–3680	O–H	The presence of hydroxyl group is indicated by a broad band indicative of hydrogen bonding. With a sharp bans at 3450 for free ligand disappearing for the complex
3080	2930	C–H	Stretching band for aromatic C–H bonds
1650	1620	C=O	Carbonyl band, resulting from conjugation with the ring double bonds, characteristic of coumarins (shifted at a lower wavenumber in the complex)
1440–1600	1450–1600	C=C	Aromatic double bonds, observed as multiple bands
1030–1390	1030–1350	C–O	Ester function bands, observed as multiple bands
840	840	C–H	Out-of-plane deformation of the benzene ring

Table 2 ^{1}H NMR data of DAPH and Ni–DAPH complex

Position	Spectral data (δ (ppm)/J coupling constant)	
	Ligand DAPH	Ni–DAPH complex
(14H)	6.25 (d, J = 9.4)	6.70 (d, J = 9.4)
(15H)	7.98 (d, J = 9.4)	7.95 (d, J = 9.4)
(17H)	7.03 (d, J = 8.5)	8.41 (d, J = 8.5)
(16H)	6.98 (d, J = 8.5)	7.32 (d, J = 8.5)

spectrum of the Ni–DAPH complex (Fig. S3B) exhibits a broad band spanning from 3100 to 3600 cm^{-1}, indicating the possible coordination of water molecules to the Ni^{2+} ion[21] (Table 1). Furthermore, the IR spectral data indicate a shift in the C=O band for the Ni–DAPH complex towards lower wavenumbers (1620 cm^{-1}) compared to the free ligand. This shift suggests that the DAPH ligand is coordinated to the transition metal through the oxygen of the carbonyl group. This result is consistent as indicated by Dehari *et al.* (2012).[21]

In addition, the intensity of the peak corresponding to the carbonyl has decreased because of electron density redistribution and reduced dipole moment change upon coordination.

4.1.3 NMR analysis. The ^{1}H-NMR spectrum of daphnetin in CD3OD (Fig. S4), shows four doublets for the aromatic protons attributed as follows: H14, 6.25 (d, J = 9.4); H15, 7.98 (d, J = 9.4); H16, 6.98 (d, J = 8.5) and H17, 7.03 (d, J = 8.5) (Table 2). Regarding the Ni–DAPH complex (Fig. S5), downfield shifts were observed for all the protons compared to the free ligand. The electron density around the coumarin changes upon coordination to the nickel center. Nickel, being a transition metal, can withdraw electron density from the ligand through σ-donation and π-backbonding. This electron withdrawal causes deshielding of the protons in the ligand, leading to a downfield shift. In addition, nickel can generate an anisotropic magnetic

environment upon coordination; hence, the ligand protons in proximity to this anisotropic field experience altered local magnetic fields, which can cause a downfield shift in the NMR signals.

4.2 Ligand structure optimization

The first step involved the optimization of the geometry for the ligand (7, 8-dihydroxycoumarin) under the aforementioned conditions. The resulting most stable geometry of the molecule is depicted in Fig. 3.

4.3 Structure of Ni–DAPH complex

To identify the most stable structure of the synthesized Ni–DAPH complex, we explored various configurations, considering all possible arrangements that could participate to the
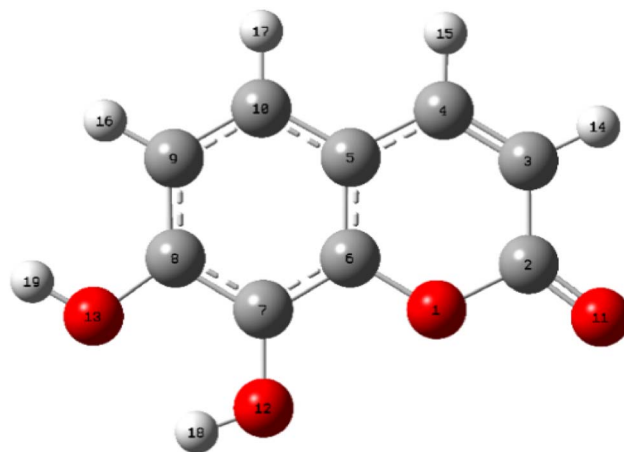

Fig. 3 Daphnetin (DAPH) optimized structure by DFT B3LYP/6-311++G (d, p), using methanol as solvent, E = −647.38 au (−406237.42 kcal mol^{-1}).
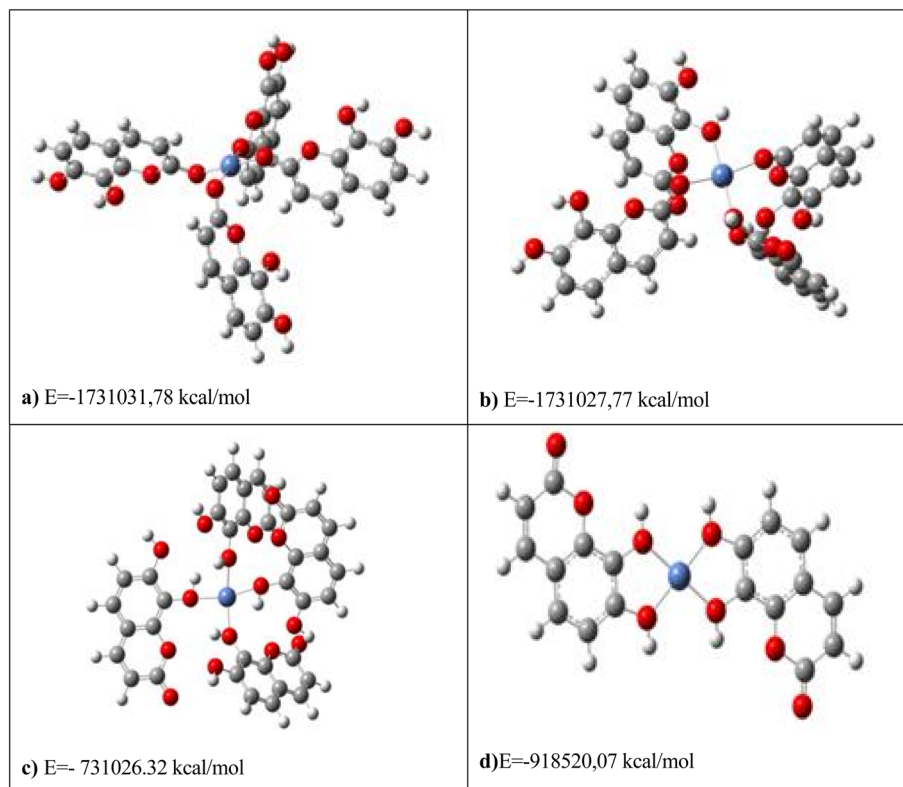
Fig. 4 Designed configurations and their energy minima for Ni–DAPH complex geometrically optimized by DFT/LANL2 DZ in gas phase: (a) four molecules of ligand bound to Ni through carbonyl groups (b) two molecules of ligands bound to Ni through OH group and 2 ligands through carbonyl group (c) four molecules of ligand bound to Ni through hydroxyl groups (d) two molecules of ligands bound to Ni through 4 hydroxyls (2 from each ligand).

formation of the complex. When closely examining the chemical structure of the ligand, we can gain valuable insights into its functional groups, bonding capabilities, and potential interaction sites with the metal center. Specifically, we can identify three charge-donor sites in the ligand: one carbonyl group and two hydroxyl groups. Taking into account that the most stable nickel complexes with L-type ligands tend to exhibit

tetradentate coordination, we proposed and evaluated four possible configurations for the complex (Fig. 4). The geometry of these complexes was optimized by DFT-LANL2DZ in the gas phase first, and with the same parameters as above. The energy minima for these complexes have been compared. It is clear from the results presented in Fig. 4, that complex 1 involving the tetracarbonyl-Ni coordination is the most stable with an
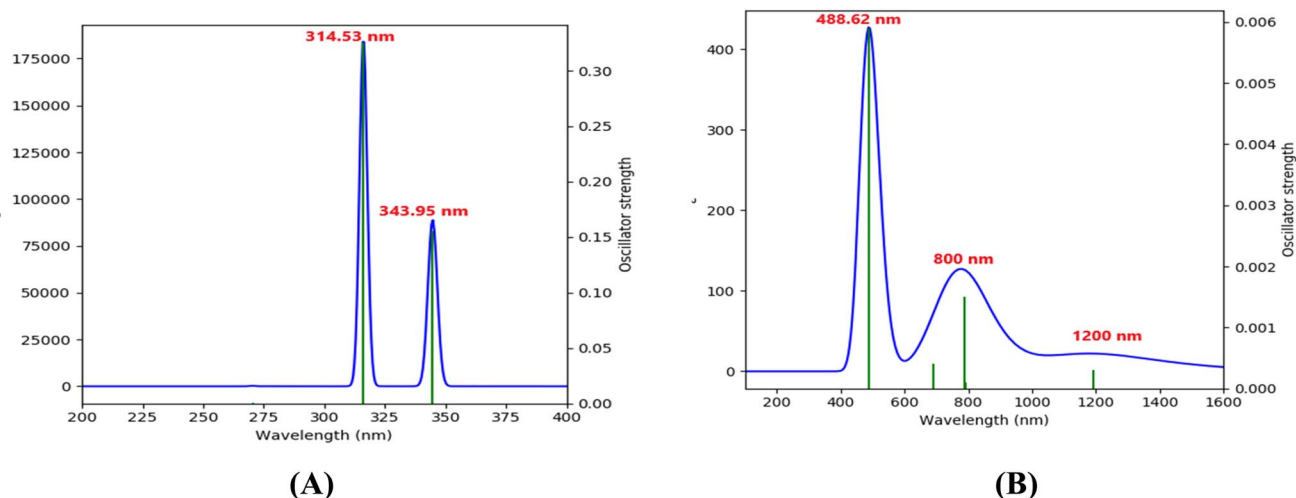

Fig. 5 UV-vis spectra of DAPH (A) and Ni–DAPH complex (B) simulated by TD-DFT/B3LYP.

energy minimum of −1731031.78 kcal mol^{-1}, followed by complex 2 and 3 with slight energy differences. Hence, the most probable structure of the Ni-DHC complex is that involving a 4 : 1 stoichiometry. The least stable configuration is that of complex 4 (stoichiometry 2 : 1), with an energy of −918520.0663 kcal mol^{-1}, a value almost equal to half that of complex 1, found to be the most stable.

The findings indicate that the geometry of the complex is tetradentate square planar, characterized by four dative bonds involving Ni–C=O. This conclusion is corroborated by the vibrational frequency analysis, which reveals a decrease in the wavenumber of the carbonyl band from 1625 cm^{-1} in the free ligand to 1619 cm^{-1} in the complex. This shift indicates the coordination of the carbonyl group to the nickel center, resulting in a weakening of the carbonyl bond due to electron donation into the metal's orbitals. Such a shift is a characteristic signature of metal–ligand interaction and provides strong evidence for the involvement of the carbonyl group in complexation.

4.4 Theoretical spectral analysis

4.4.1 TD-DFT UV-vis absorption spectra. The electronic absorption spectrum of daphnetin was determined through TD-DFT calculations (Time Dependent-DFT) method using B3LYP/(6-311G)++(d, p) as basis, The UV-vis spectrum (Fig. 5A) of the
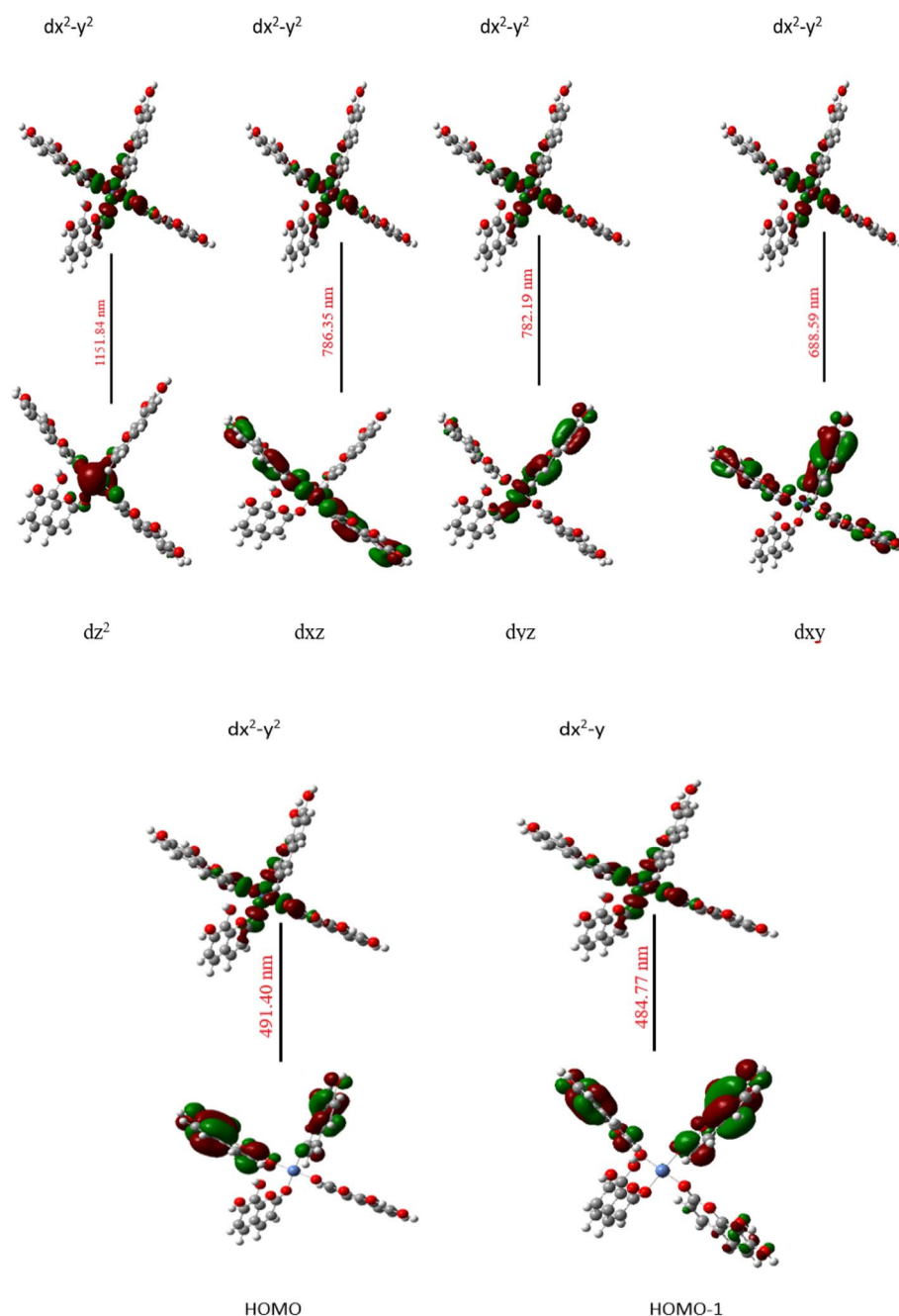

Fig. 6 TD-DFT/B3LYP/LANL2DZ calculated electronic absorption transitions (1200−400 nm) and selected FMO orbitals of Ni−DAPH complex.

ligand displayed two bands, the first one at λ max = 314.53 nm that is equivalent to a π– π^* transition or K band and the second one, at 343.95 nm, corresponds to a π– π^* transition or B band of a substituted aromatic derivative.

The UV-Vis absorption spectrum (Fig. 5B) of the Ni–DAPH complex exhibits distinct peaks characteristic of its electronic transitions. Table S1 provides valuable insights into the electronic transitions. Here, the metal's dx^2-y^2 orbital serves as the LUMO (Fig. 6). The analysis focuses on six primary electronic states characterized by their excitation energies: 1.0764 eV, 1.5767 eV, 1.5851 eV, 1.8006 eV, 2.5231 eV, and 2.5576 eV. The contribution values quantify the relative changes in electron density within the orbitals involved in these transitions. For the first state, a high positive contribution of 104.5% signifies a substantial increase in electron density in the orbital during excitation. In contrast, a negative contribution of −10.3% reflects a loss of electron density from the corresponding orbital. The initial transitions, corresponding to wavelengths; λ = 1151.44 nm and λ = 786.35 nm in the near-infrared region, exhibit low oscillator strengths (f = 0.0003 and f = 0.0001 respectively), indicative of weakly allowed or forbidden transitions. Despite their low intensity, the dominant contributions from higher-energy orbitals, such as H−10 → L (63.5%), sustain the transitions, albeit weakly. Lower-energy transitions (longer wavelengths) typically correspond to d–d transitions within the nickel d orbitals. Conversely, higher-energy states (2.5231 eV and 2.5576 eV) display stronger oscillator strengths (f = 0.0057 and f = 0.0010), suggesting more allowed transitions with significant orbital overlap. These states involve prominent contributions such as H → L (96.3%) and H−1 → L (69.0%), indicative of substantial electronic excitations. The corresponding shorter wavelengths (λ = 491.40 nm and λ = 484.77 nm) and higher excitation energies point to stronger absorptions, likely attributed to ligand-to-metal charge transfer (LMCT) and $\pi \rightarrow \pi^*$ transitions.

Fig. 7 Solvatochromic effect for Ni–DAPH complex simulated by TD-DFT/B3LYP.

4.4.2 Solvatochromic effect. The solvent can affect the wavelength of light absorbed by a compound because it interacts with the electronic structure of the compound, often influencing its excited states. This phenomenon, where the absorption maximum shifts depending on the solvent, is known as the solvatochromic effect.

Polar solvents like DMSO (dimethyl sulfoxide) and water are highly polar, compared to methanol.

When a solvent is polar, it can stabilize the excited state of the molecule more than the ground state due to dipole–dipole interactions. In most cases, the excited state of a molecule has more charge separation (*i.e.*, is more polar) than its ground state. Consequently, polar solvents have the ability to stabilize the excited state, lowering its energy and hence causing a bathochromic shift (Fig. 7).

4.4.3 Infrared spectra. The vibrational frequencies of DAPH and Ni–DAPH complex were calculated with the Gaussian 09 program using the DFT method with B3LYP/(6-311G)++(d, p)/LANL2DZ basis sets. In the Table 3, we represented a tentative assignment of the main functional groups in the ligand and the complex. It can be seen a strong agreement between the experimental and computational results concerning the vibrational frequencies. In addition, when comparing the wavenumbers of the complex and those of the ligand, we can see some shifts especially a downshift for the C=O group indicating that this functional group was indeed the most favorable binding site between the ligand and the metal. It can therefore be suggested that the coordination between DAPH and Nickel took place *via* the oxygen of the carbonyl of the benzopyrone ring (Fig. S6).

4.4.4 Proton NMR spectra. ^1H NMR is a powerful technique for studying coordination complexes, offering insights into coordination sites (through chemical shifts), changes in ligand symmetry, possible chelation and hydrogen bonding effects. Coordination to nickel may induce conformational changes in daphnetin structure. If the geometry changes, the spatial arrangement of electron density around certain atoms (such as aromatic protons or hydroxyl groups) could also change, altering the shielding and resulting in a shift of NMR signals.

Table S2 represents the proton NMR chemical shifts for the ligand and the complex computed with DFT-GIAO using methanol as solvent.
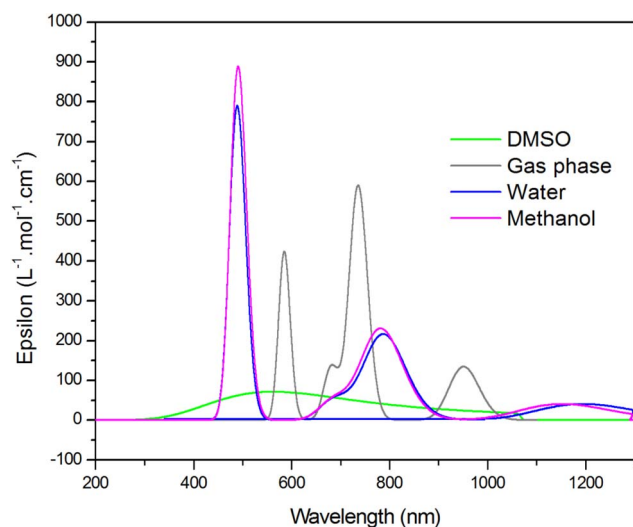
Table 3 Calculated vibrational frequencies (cm^{-1}) for ligand DAPH and the Ni–DAPH complex

Wavenumber $\bar{\upsilon}$ (cm^{-1})		
Ligand	Complex	Assignment
3648–3550	3646–3720	OH
3221	3221–3283	C–H
1625	1619	C=O
1436–1612	1421–1607	C=C
1046–1311	1016–1019	C–O
	1060–1323	
869	845	C–H deformation (aromatic ring)

Table 4 Comparison of chemical shifts in the ligand and complex for the most deshielded protons in the complex

Protons of the ligand	δ (ppm)	Protons of Ni–DAPH complex	δ (ppm)	$\Delta\delta$ (ppm)
14H	5.982	12H	8.104	2.122
		31H	8.224	2.242
		50H	6.330	0.348
		69H	9.208	3.226
15H	7.3238	15H	8.157	0.8332
		34H	8.109	0.7852
		53H	7.658	0.3342
		72H	7.959	0.6352

The computed NMR spectrum of DAPH (Fig. S7 inset), shows 4 signals in the aromatic region, corresponding to protons, H14 (5.982 ppm), H15 (7.3238 ppm), H16 (6.426 ppm) and H17 (6.616 ppm), besides two signals for the protons of the OH groups, 18H (5.692) and 19H (4.752 ppm).

Upon reacting with the nickel cation to create a tetradentate complex, the four protons (14H–17H) assumed distinct positions within the complex. The discrepancy in chemical shifts between the complex and the free ligand indicates that all protons, including those in the hydroxyl groups, have undergone a downfield shift. This suggests that these protons now reside in a different environment (as depicted in Fig. S7), resulting in deshielding at their NMR positions.

It is worth noting that the closer to the nickel center the more the protons were deshielded. This is probably due to the influence of unpaired electrons from the metal ion, which creates a local magnetic field that impacts nearby nuclei through direct magnetic effects of unpaired electrons, redistribution of electron density upon coordination; magnetic anisotropy of the metal center's field and dipolar interactions.

Additionally, the protons 14H (5.982 ppm) and 15H (7.3238 ppm) of the benzopyrone ring in the free ligand, now observed in the complex at new positions: 12H (8.104 ppm), 31H (8.224 ppm), 50H (6.33 ppm), 69H (9.208 ppm), 15H (8.157 ppm), 34H (8.109 ppm), 53H (7.658 ppm), and 72H (7.959 ppm) have undergone the most significant downfield shifts, ranging from 0.3342 to 3.226 ppm (Table 4). These significant downfield shifts are likely due to the proximity of these protons to the strongest electron-donating site on the coumarin, specifically the O=C–O group. Upon coordination with the metal center, electron density around the coumarin ring, particularly near the O=C–O group, is redistributed. This change in electron density results in reduced shielding of nearby protons, shifting their resonances downfield. The $\Delta\delta$ (ppm) for all the other protons were less than 1 ppm.

The comparison of these results with experimental ones yielded differences less than 1 ppm, varying from 0.009 to 0.678 for five protons. For the other 3 protons $\Delta\delta$ (ppm) varied from 1.42 to 2.05 ppm (Table S3). Differences between observed and computed NMR chemical shifts can arise from several factors. First, DFT calculations often use an implicit solvent model, which does not fully capture specific solute–solvent interactions present in experimental conditions, potentially leading to peak shifts. Second, the experimental NMR spectrum represents an
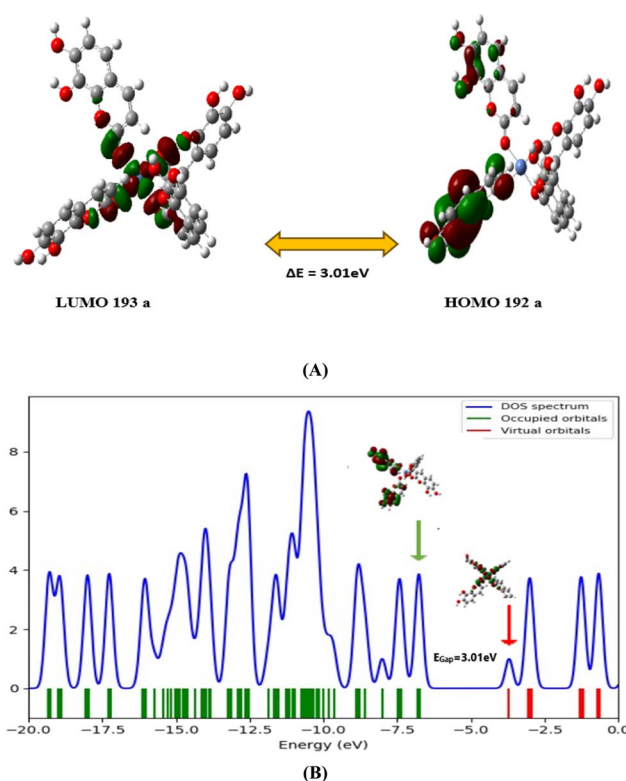
average over all accessible conformations of the molecule in solution, while theoretical calculations are typically performed on a single, energy-minimized structure. Additionally, the choice of functional and basis set in the DFT method can significantly influence the accuracy of the predicted chemical shifts and other molecular properties.[27]

4.5 Study of molecular orbitals

The study of the Highest-Occupied Molecular Orbital (HOMO) and Lowest-Unoccupied Molecular Orbital (LUMO) frontier orbitals is highly valuable for understanding the reactivity of molecules, as they provide insights into the most reactive positions of the system and various aspects of a reaction.

According to the frontier orbital theory in Density Functional Theory (DFT), a molecule with a higher HOMO energy undergoes electron donation reactions more rapidly. Conversely, a molecule with a lower LUMO energy exhibits a higher electron accepting ability.[28–30] Compounds with a low energy gap between the HOMO and LUMO energies ($\varepsilon G = E_{HOMO} - E_{LUMO}$) and a low LUMO energy are characterized by high reactivity.

The $E_{HOMO} - E_{LUMO}$ gap, also known as chemical hardness, represents the resistance of a molecular system to electron transfer, whether it involves electron gain or loss. It is also a measure of the stability of a molecule.[31] Table S4 presents the energies of the HOMO and LUMO orbitals, the $E_{HOMO} - E_{LUMO}$ energy gap, and other calculated properties for the Ni–DAPH complex.

LUMO 193 a $\Delta E = 3.01 eV$ HOMO 192 a

(A)

(B)

Fig. 8 HOMO and LUMO frontiers orbitals (A) and Total density of states (TDOS) for Ni–DAPH complex (B).

The localization of the frontier molecular orbitals HOMO and LUMO on the atoms of the Ni–DAPH complex, as well as the energy difference between the HOMO and LUMO orbitals (energetic gap), are depicted in Fig. 8.

The HOMO orbitals of the Ni–DAPH complex are localized on the π bonds of the four rings on the left side of the complex, as well as on the oxygen atoms O-71, O-70, O-73, O-75, O-14, O-13, O-16, and O-18. These regions correspond to the nucleophilic sites of the Ni-DAPH complex.

On the other hand, the LUMO orbitals in the ground state predominantly reside at the center of the complex, particularly on the Ni^{2+} ion. They are also distributed between the atoms C-10 = O-14, O-71 = C-67, O-33 = C-29, O-52 = C-48, O-70-C-61, O-32-C-23, C-48-C-49, O-13-C-4, and the oxygen atom O-51. These regions represent the electrophilic sites of the Ni-DAPH complex.

Fig. 8 represents the total density of states spectrum (TDOS) obtained using the Gauss Sum software. Gauss Sum typically sets the highest occupied molecular orbital (HOMO) as the reference point. Therefore, energies below this point represent occupied states, while energies above this point represent unoccupied states.

The gap between the HOMO and the LUMO (lowest unoccupied molecular orbital) represents the 3.01 eV energy gap and will be visible as a region without any states between the highest occupied peaks and the lowest unoccupied peaks. The HOMO will be the highest energy state with a significant peak on the left side (occupied states), while the LUMO will be the first peak on the right side (unoccupied states). The difference in energy between these peaks gives the energy gap, which is 3.01 eV.

A gap of 3.01 eV, indicates that the complex will likely be a poor conductor at room temperature, behaving as a semiconductor or insulator. In addition, the complex may exhibit photoactivity in the visible region, particularly in the blue-violet range around 412 nm, making it potentially useful for optical applications.

4.6 Nonlinear optical characterization of the Ni-DAPH complex

Transition metal complexes are of special interest due to their unique electronic structures, which enable rich photophysical and electronic behaviors. The presence of metal centers with d-orbitals can enhance electronic delocalization and introduce charge-transfer interactions that are essential for high hyperpolarizability; a key indicator of strong nonlinear optical (NLO) response.

Exploring the NLO properties including dipole moment, polarizability, first-order hyperpolarizability, and second-order hyperpolarizability of these complexes not only advances fundamental knowledge of structure–property relationships in coordination chemistry but also opens avenues for developing advanced materials for optical switching, frequency doubling, telecommunications, medical imaging, laser technology, and data storage.

The nonlinear optical response of the daphnetin complex has been investigated in both static and dynamic states. Static properties are more indicative of linear and second-order NLO effects, while dynamic properties are critical for understanding frequency-dependent and higher-order NLO effects.[32] Our results, summarized in Table S5, highlight the promising potential of this coordination complex for various applications. The theoretical calculations of polarizability and hyperpolarizability are presented in electrostatic units (esu).

The dipole moment, polarizability (α tot) and hyperpolarizabilities (β and γ) are important parameters in the study of molecular nonlinearity and optical properties. Here are the formulas commonly used to calculate these quantities:

$$\mu = (\mu^2 \text{ x} + \mu^2 \text{ y} + \mu^2)^{1/2}$$

$$\alpha = (\alpha_{xx} + \alpha_{yy} + \alpha_{zz})/3$$

Where α_{xx}, α_{yy} and α_{zz} are the components of the polarizability tensor.

$$\beta = (\beta2 \text{ x} + \beta2 \text{ y} + \beta2 \text{ z})^{1/2}$$

$$\gamma = [(\gamma_{xxx} + \gamma_{yyy} + \gamma_{zzz} + 2 (\gamma_{xxyy} + \gamma_{xxzz} + \gamma_{yyzz})]/5$$

Table S5 summarizes the values of the factors in (electrostatic unit) esu.

The dipole moment measures the separation of positive and negative charges within a molecule, indicating molecular polarity. The higher dipole moment obtained (13.63 debye) suggests greater polarity, which can influence solubility and reactivity.[31] Higher values of static polarizability 10.31×10^{-23} esu and anisotropy of polarizability (2.21×10^{-23} esu); indicate that the molecule can become more polarized, impacting interactions with external fields and other polarizable molecules.

Similar to $\Delta\alpha$ (0.0), anisotropy of dynamic polarizability (2.79×10^{-23} esu), indicates the directional dependence of polarizability under dynamic conditions, at a given frequency. This could relate to the molecule's optical properties.

Lower value (9.44×10^{-23}) of dynamic polarizability suggests less response in oscillating fields compared to the static case. The higher β and β ($-2 \omega, \omega, \omega$) values indicate a stronger nonlinear response and an enhanced response at this combination of frequencies (potentially useful in applications requiring specific harmonic generation)n respectively. The slightly higher γ value (28.60×10^{-35} esu) indicates an increased third-order NLO response at that frequency, which can be important for applications like all-optical switching and frequency stabilization.

4.7 Atomic charges and ESP map

The calculation of atomic charges is significant in quantum calculations applied to molecular systems, due to their influence on properties like dipole moment, polarizability, and electronic structure.[26]

The charge distribution of the Ni–DAPH complex was assessed using the B3LYP/LANL2DZ level of theory. The results,

depicted in Fig. 9A, reveal that positive charges are primarily localized on the hydrogen atoms, while the carbon atoms exhibit both positive and negative charges.

The oxygen atoms of the hydroxyl groups (O-18, O-16, O-37, O-35, O-56, O-54, O-73, and O-75) exhibit more negative charges compared to the oxygen atoms of the benzopyrone rings due to the presence of intramolecular hydrogen bonds, such as O18-H19, *etc.* This indicates that the oxygen atoms of the hydroxyl groups are more nucleophilic than the oxygen atoms of the pyrone ring. Additionally, the atoms O-14, O-33, O-52, and O-71 coordinated with the Ni^{2+} ion display negative atomic charges. The Ni atom itself exhibits the highest positive atomic charge (0.515). This signifies that the Ni^{2+} ion is the most electrophilic site within the complex.

It is important to note that these results were obtained for the complexation between DAPH and nickel using water as the solvent. Changes in parameters such as the ligand–metal coordination capacity are likely to occur when the solvent polarity is changed.[26]

Molecular electrostatic potentials (MEPs) are widely recognized as valuable indicators of molecular reactivity. The calculated

MEP is especially useful for analyzing noncovalent interactions.[33] To explore the reactive regions involved in both electrophilic and nucleophilic interactions, electrostatic potential maps were generated for the optimized geometry of the Ni–DAPH complex at the B3LYP/LANL2DZ level. The total electron density, displayed on the electrostatic potential surface, is shown in Fig. 9B.

The electrostatic potential (ESP) map of this metal complex reveals a balanced distribution of charge due to significant electron donation from the carbonyl (C=O) ligands to the central metal ion. In this complex, each carbonyl oxygen donates a lone pair to form a dative bond with the metal, effectively reducing the metal's formal charge. This electron donation is reflected in the ESP map, where the metal center appears less intensely positive (likely light blue to greenish-blue), indicating a moderated electron deficiency. The carbonyl oxygen atoms, having donated electron density, exhibit neutral to slightly negative potential, which appears in green or yellow shades on the map, rather than a strongly negative region. This more uniform ESP distribution suggests a stable coordination environment, with the complex exhibiting reduced reactivity towards nucleophiles, as the metal's charge is
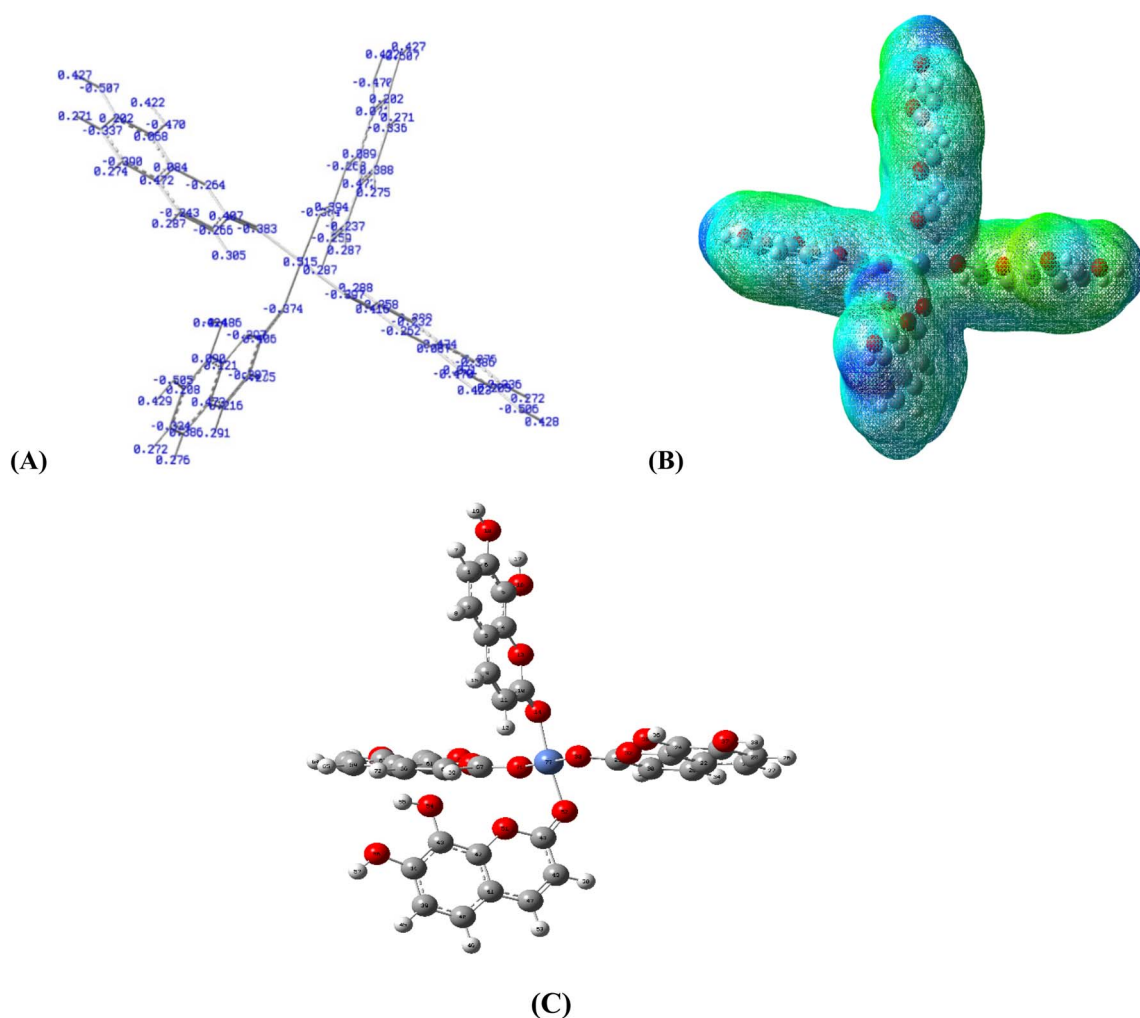

Fig. 9 Atomic charge distribution (A) and electrostatic potential (MEP) (B) for Ni–DAPH complex (C) computed by DFT at B3LYP/LANL2DZ level of theory.

significantly neutralized by the dative bonds. Overall, the ESP map highlights the stability and mild reactivity of the complex, with a balance that could make it suitable for selective interactions, such as in catalytic applications or controlled binding scenarios, where extreme charges might be less favorable.

4.8 Natural bond orbital analysis (NBO)

The dative bond (donor–acceptor interactions) in the Ni–DAPH complex was studied using the natural bonding orbital (NBO) analysis which is a powerful method used in quantum chemistry to examine the bonding in a molecule.[34] A useful aspect of the NBO analysis method is that it provides information about interactions in filled and virtual orbital spaces, which could improve the analysis of intra- and intermolecular interactions.[35]

The natural population analysis (NPA) of the Ni–DAPH complex reveals that the most electronegative charges are concentrated on the oxygen atoms bonded to the Ni atom. Notably, the natural charge of the Ni ion decreases significantly from +2.0 in its free state to +0.92 upon complexation, indicating substantial electron transfer from the oxygen orbitals. Furthermore, the natural electronic configurations (NEC) of the free oxygen and nickel ions were $(2s^2 2p^4)$ and $(4s^2 3d^8 4p^0 5p^0)$, respectively. After complexation, the NEC of the nickel ion becomes Ni 4s (0.26) 3d (8.55) 4p (0.06) 5p (0.21), showing a notable increase in orbital occupancy compared to the free ion. This enhanced occupancy, along with the strong intramolecular interactions between the ligand and the metal, contributes to the increased stability of the complex. The occupancy of the 3d orbitals and their corresponding energies for Ni in the Ni–DAPH complex are detailed in Table S6. Notably, the anti-bonding orbital d_{x2-y2} exhibits the highest interaction energy (-0.2548 eV) and the lowest occupancy (0.76331), indicating it as the lowest unoccupied molecular orbital (LUMO) and significantly less stable compared to other orbitals (d_{z2}, d_{xz}, d_{yz}, d_{xy}). This observation elucidates the interactions between the orbitals (donor) on the coordination atom of the ligands and the metal d orbitals (acceptor).

The d_{xy} orbital exhibits a lower energy level (-0.38413 eV) compared to the d_{xz}, d_{yz}, and d_{z2} orbitals, establishing it as the most stable orbital with a maximum occupancy of (1.98186). Additionally, the observed angles of 88.763°, 90.045°, 90.352°, and 90.798° for O14NiO71, O71NiO52, O52NiO33, and O33NiO14, respectively, indicate symmetry within the complex structure. This symmetry leads to the determination of the

Table 5 Donor–acceptor interactions and their stabilization energies in NBO analysis for Ni-DAPH complex

Donor	Acceptor	Distances (Å)	$E^{(2)}$ kcal. mol^{-1}
LPO14	LP*Ni 77	1.894	36.07
LPO33	LP*Ni 77	1.886	35.92
LPO52	LP*Ni 77	1.895	37.97
LPO71	LP*Ni 77	1.892	32.73
Total energy			142.69

order of the 3d orbitals as $d_{x2-y2} > d_{z2} > d_{xz} > d_{yz} > d_{xy}$. These findings align with existing literature.[36–39]
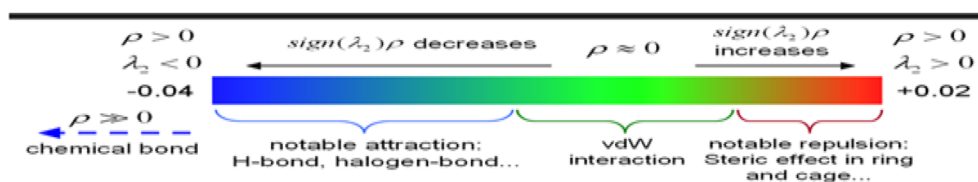
In the title complex, the NBO analysis explored donor–acceptor interactions through second-order perturbation theory. The analysis identified electron donors, associated acceptors, intermolecular distances, and the stabilization energies of E^2 interactions within the complex. The compiled results are accurately presented in Table 5. The intermolecular distances between occupied and unoccupied orbitals, determined through NBO analysis of the Ni–DAPH complex, are as follows: O14-Ni: 1.894 Å; O33–Ni: 1.886 Å; O52-Ni: 1.895 Å; and O71–Ni: 1.892 Å. Notably, these distances of the (Ni–O) bonds are nearly identical, suggesting uniformity in the strong intramolecular interaction between the ligand and the metal. This interaction contributes to a heightened stabilization of the complex structure.

Table 5 presents the second-order disruption energies $E^{(2)}$ (often called stabilization energies or interaction energies) of the NBOs interacting between the donor (oxygen) and acceptor (nickel ion) of the Ni–DAPH complex. The total $E^{(2)}$ energy was found to be 142.69 kcal.mol^{-1}. A high $E^{(2)}$ value is linked to a strong intramolecular charge transfer.[35,40,41] The interaction energies are in the range 32.73–37.97 kcal. mol^{-1}. The substantial interactions are particularly seen between lone pairs LP (O14) and LP*Ni (36.07 kcal.mol^{-1}), LP (O33) and LP*Ni (35.92 kcal.mol^{-1}), LP (O52) and LP*Ni (37.97 kcal.mol^{-1}) and LP (O71) and LP*Ni (32.73 kcal.mol^{-1}). The above-mentioned hyper-conjugative interactions are the most responsible for Ni–DAPH complex stability.[41,42]

4.9 Non-covalent interactions (NCI)

NCI serves as a tool for visualizing and identifying non-covalent interactions, including van der Waals interactions, hydrogen bonds, and steric effects. The index relies on density and its
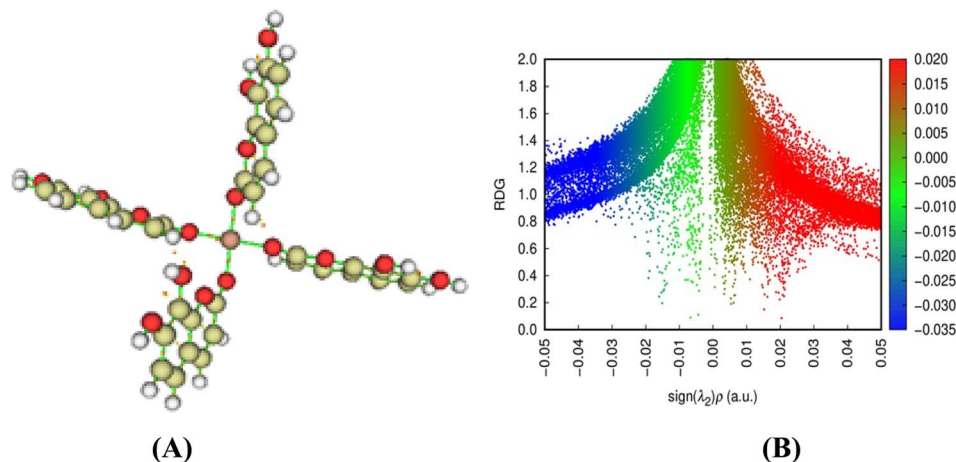
NCI Index

Fig. 10 QTAIM (BCPs) 3D (A) and RDG iso-surface 2D (B) plots of investigated complexes.

derivatives. Examining the plot in Fig. 10, it is evident that van der Waals interactions took place between two ligand molecules in proximity to the coordination center, where robust attractive interactions were also noted. Additionally, a steric effect manifested in the benzopyrone ring of the ligand.

Remarkable repulsive interaction (red) is observed between O33 and O41 at 2.692 Å and between O14 and O71 at 2.648 Å.

The NCI analysis showed the presence of van der Waals, robust attractive, steric effect and repulsive ligand–ligand and/or ligand –metal interactions.

4.10 Topological parameters calculated by quantum theory of atoms in molecules (QTAIM)

In contemporary times, Bader's theory, known as Quantum Theory of Atoms in Molecules (QTAIM), has become a robust methodology for investigating diverse chemical interactions by analyzing electron density topology. These interactions encompass ionic, covalent, and hydrogen bonds. Additionally, QTAIM is increasingly used to analyze various subtler interaction types, such as van der Waals forces or metal–metal interactions.[43]

As per QTAIM, the evaluation of chemical bonding and interactions requires an analysis of electron density ρ (r) and its Laplacian $\nabla^2(\rho)$, the ellipticity, Hessian Eigen values, potential V(r), kinetic G(r), and total energy densities H(r) at the bond critical points (BCPs). A higher electron density at BCPs signifies enhanced structural stability. A closed shell interaction, as

observed in ionic and hydrogen bonds, is characterized by a positive $\nabla^2(\rho)$ value at BCPs, while covalent interactions are present for negative $\nabla^2(\rho)$ values.[44]

The dominance of potential energy and concentration of a negative charge occurs when the Laplacian value is negative. Conversely, the dominance of kinetic energy and a depletion of negative charge occur when the Laplacian value is positive.

The virial theorem establishes a connection between G(r) and V(r) of the local electron in relation to $\nabla^2(\rho)$ as expressed in the equation:

$$\nabla^2(\rho)/4 = 2Gc + Vc$$

The combination of G(r) and V(r) equals the total energy density H(r). The sign and magnitude of the total energy density H(r) serve as valuable indicators revealing the nature of a bonded chemical interaction.[43]

A negative H(r) signifies a covalent interaction, whereas a positive value indicates an ionic interaction. However, in metal–ligand and metal–metal bonding, H(r) typically tends to be negative and close to zero, with $\nabla^2(\rho) > 0$. At bond critical points (BCPs), positive and negative $\nabla^2(\rho)$ values indicate closed-shell and shared-electron interactions, respectively.[42]

The results presented in Table 6 reveal lower electron density values (ranging from 0.088 to 0.091 a. u.) and higher positive Laplacian values $\nabla^2(\rho)$, increasing from +0.604 to +0.613 a. u. These findings strongly suggest the presence of ionic bonding. However, the observed negative H(r) values at bond critical

Table 6 Topological parameters in (a.u): electron density ρ(r) Laplacian of electron density $\nabla^2\rho$(r), ELF and LOL. Energetic topological parameters: electron kinetic energy density G(r), electron potential energy density V(r), total electron energy density H(r)

Contacts	D(Å)	ρ (r)	$\nabla^2(\rho)$	G(r)	K(r)	V(r)	H(r)	ELF	LOL
$O_{33}\cdots Ni_{77}$	1.886	0.091	0.613	0.168	0.015	−0.184	−0.015	0.089	0.238
$O_{52}\cdots Ni_{77}$	1.894	0.090	0.604	0.166	0.015	−0.180	−0.015	0.089	0.239
$O_{71}\cdots Ni_{77}$	1.892	0.088	0.607	0.165	0.013	−0.178	−0.013	0.085	0.233
$O_{14}\cdots Ni_{77}$	1.894	0.088	0.608	0.165	0.013	−0.132	−0.013	0.085	0.234

points (BCPs) suggest the existence of a certain degree of covalency.

ELF, or the Electron Localization Function, is employed for assessing the localization of electrons between chemically bonded atoms, serving as a straightforward and valuable quantum-mechanical approach.

The ELF is plotted within the interval (0, 1) and elucidates the Pauli repulsion effect occurring at the interaction point of two atoms. The ELF value serves as a representation of the likelihood of finding two electrons with the same α-spin within the specified space, indicating Pauli's repulsion. Consequently, ELF can be employed as an effective tool for characterizing bonding, particularly in metal–ligand interactions.[45]

In the case of purely ionic bonding, elevated ELF values are noted in proximity to the nuclei, approaching a value of approximately 1.0, while remaining significantly low (around 0) in the interstitial region. In the case of covalent bonding, The ELF values that connect two atoms may vary from 0.6 to 1.0, contingent upon the bond's strength.[46]

As indicated by the findings presented in the Table 6, the ELF values obtained for the Ni–DAPH complex are 0.085 and 0.089 for Ni–O bonds. This suggests that pure ionic bonding has occurred in the interstitial region, away from the nuclei.

As for the localized orbital locator (LOL)[47] our values fall within the range 0–1 but are smaller than 0.5 indicating a region for delocalized electrons.

4.11 Antioxidant activity

Antioxidant activity is crucial in pharmacology because oxidative stress, caused by an imbalance between free radicals (reactive oxygen species, ROS) and antioxidants, plays a very important role in the pathogenesis of various diseases such as cancer, cardiovascular diseases, diabetes, neurodegenerative disorders (e.g., Alzheimer's, Parkinson's), and chronic inflammation. Antioxidants mitigate this stress by neutralizing ROS, thus protecting cells from damage to lipids, proteins, and DNA and maintaining physiological function, which is important for disease prevention and therapeutic interventions.

A key parameter for assessing the antioxidant or anti-radical activity of both natural and synthetic compounds is the bond dissociation enthalpy (BDE). BDE indicate the amount of energy necessary to cleave a particular bond within a molecule, resulting in the generation of radicals.[48,49]

In this study, the optimization energies of various neutral and radical species (both ligand and complex) were computed using density functional theory (DFT). The B3LYP hybrid functional was employed along with the LANL2DZ and (6-311G)++(d, p) basis sets, with methanol as the solvent, to determine the BDE values.

To compare the antioxidant activity of the Ni–DAPH complex with that of the DAPH ligand, the hydrogen atom transfer (HAT) mechanism was studied. The HAT mechanism involves the transfer of a hydrogen atom from the antioxidant molecule to an oxidative radical in a single step:
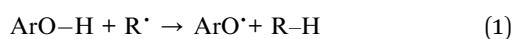
$$\text{ArO–H} + \text{R}^{\cdot} \rightarrow \text{ArO}^{\cdot} + \text{R–H} \tag{1}$$

Table 7 BDE in KJ mol^{-1} obtained at B3LYP/6-311++G (d, p) and LANL2DZ level of theory, in MeOH, for DAPH and Ni–DAPH^{a}

OR site of DAPH	BDE (kJ mol^{-1})	OR site of Ni–DAPH complex	BDE (kJ mol^{-1})
7-OH	360.83	5-OH	336.29
		24-OH	336.46
		43-OH	336.06
		62-OH	335.70
8-OH	349.32	6-OH	329.63
		25-OH	330.34
		44-OH	331.54
		63-OH	328.28

^{a} The table compares the bond dissociation energies (BDE) at specific hydroxyl (–OH) sites of a ligand (DAPH) and its corresponding complex (Ni–DAPH).

Bond dissociation energies (BDEs) were evaluated to explore the HAT mechanism. Importantly, a lower BDE is associated with enhanced antioxidant activity, making the reaction with free radicals more favorable.

The BDE in the HAT mechanism was determined utilizing the subsequent equation:

$$\text{BDE} = \text{H (ArO}^{\cdot}) + \text{H(H}^{\cdot}) - \text{H(ArOH)} \tag{2}$$

The enthalpy (H) of the hydrogen radical (H$^{\cdot}$) in vacuum has been calculated, yielding a value of -1318.75 kJ mol^{-1}.

ΔSolv H(H$^{\cdot}$) value in methanol is taken from the study carried out by Ján Rimarčík et al.[50]

The enthalpy of dissociation of the hydrogen bond (BDE) of the DAPH ligand and Ni–DAPH complex studied are presented in Table 7.

The BDE values of 7-OH and 6-OH for the ligand 7,8-di-hydroxycoumarin (DAPH), are reported as 360.828 kJ mol^{-1} and 349.323 kJ mol^{-1}, respectively. The larger BDE for the ligand suggests that it is more resistant to bond dissociation before it forms a complex.

For the complex (Ni–DAPH), BDE at various hydroxyl sites are shown, with lower values ranging from 328.28 kJ mol^{-1} to 336.46 kJ mol^{-1}. The minimum bond dissociation energy (BDE) of 328.28 kJ mol^{-1} was recorded for 63-OH making it the most reactive site for antioxidant activity within the complex, followed by 6 –OH (329.63 kJ mol^{-1}), 25-OH (330.34 kJ mol^{-1}) and 44-OH (331.54). The C5–OH, C24–OH, C43–OH, and C62–OH sites have almost identical BDE values, reported as 336.29, 336.46, 336.06, and 335.70 kJ mol^{-1}, respectively, suggesting that these OH groups exhibit comparable stability and probability of H atom donation. The similar BDE values likely arise from the symmetry of the complex. Since it is a square planar complex with the same ligand coordinated at multiple sites, the environment surrounding each hydroxyl group (–OH) is quite uniform. This structural symmetry leads to nearly identical interactions between the metal center and the ligand at each hydroxyl site, which explains the minimal differences in BDE values. The consistency in the ligand coordination across these

sites contributes to the small variations observed in the bond dissociation energies (BDE).

The BDE values for these sites in the complex are consistently reduced compared to those of the free ligand, indicating that complexation weakens the bond strength of the hydroxyl groups. This reduction in BDE suggests that the metal–ligand interaction alters the electronic environment, making it easier for the hydroxyl groups to dissociate. The uniformity of the BDEs across multiple hydroxyl sites in the complex further implies that many of these –OH groups are capable of participating in hydrogen donation, thereby enhancing the compound's overall antioxidant capacity. This capacity is crucial, as hydrogen donation is a key mechanism in neutralizing free radicals, an important factor in antioxidant activity.

Furthermore, coordination with the metal in the complex enhances its electronic properties, facilitating redox reactions and contributing to its superior antioxidant behavior. This metal–ligand interaction can stabilize reactive intermediates and lower activation energy barriers for oxidation and reduction processes, which are crucial for antioxidant activity.

The ability of the metal to participate in electron transfer can also increase the overall efficiency of the antioxidant response, making the complex more effective in neutralizing free radicals compared to the free ligand. Studies have shown that metal coordination can significantly affect the reactivity and stability of hydroxyl groups, which are essential for donating hydrogen atoms in the antioxidant mechanism. This synergy between the metal and the ligand not only enhances antioxidant capacity but also provides a potential pathway for developing more effective antioxidant agents in pharmaceutical applications.[51]

4.12 Molecular docking

Molecular docking has become a crucial tool in drug design for investigating and understanding how ligands interact with target proteins.[52,53] This technique offers valuable insights into binding mechanisms, highlighting the spatial and energetic compatibility between a potential drug and its biological target. By simulating binding energies, it aids in predicting the stability of complexes and plays a key role in optimizing therapeutic candidates.[54–56] In this molecular docking study, our objective is to evaluate the antioxidant activity of the synthesized ligand and its complex by investigating its interaction with two important HEME-enzymes that play a role in defending against oxidative stress: CCP (cytochrome C peroxidase, PDB ID: 2X08)[57] and APX (ascorbate peroxidase, PDB ID: 1OAF).[58] Using the crystal structures of these enzymes, retrieved from the Protein Data Bank,[59] we performed docking simulations to identify potential binding modes and assess interaction energies.

This work is part of a growing interest in the antioxidant properties of nickel complexes, particularly with regard to their interaction with CCP and APX, known to play a crucial role in neutralizing hydrogen peroxide (HOO$^\bullet$) and reducing oxidative stress. These nickel complexes demonstrate significant antioxidant properties, acting effectively to scavenge free radicals and mitigate oxidative stress.[60,61] CCP and APX play crucial roles in the degradation of hydrogen peroxide (HOO$^\bullet$), contributing to cellular protection against oxidative damage. While CCP uses cytochrome c as an electron donor, APX employs ascorbate for the same function. When these enzymes are dysfunctional, an accumulation of HOO$^\bullet$ can occur, leading to the generation of free radicals and causing significant cellular damage. Meanwhile, antioxidants play a protective role by stabilizing free radicals and minimizing the deleterious effects of oxidative stress.[62]

The results obtained, in our case, show that both the ligand and its nickel-based complex interact effectively with the active sites of CCP and APX, suggesting a potential for stabilizing free

Table 8 Binding affinity and RMSD values of the different poses of DAPH and Ni-DAPH complex in the active site of 2X08 and 1OAF enzymes

| PDB code | Mode | DAPH | | | Ni–DAPH complex | | |
		Affinity (kcal mol^{-1})	Dist from RMS dl.b	Best mode RMSD du.b	Affinity (kcal mol^{-1})	Dist from RMS dl.b	Best mode RMSD du.b
CCP (2X08)	1	−6.0	0.000	0.000	−9.5	0.000	0.000
	2	−5.9	14.755	15.339	−9.5	0.481	8.519
	3	−5.9	22.984	25.594	−9.0	0.822	7.513
	4	−5.8	23.033	25.668	−9.0	3.620	7.998
	5	−5.8	23.546	25.801	−9.0	0.339	6.904
	6	−5.8	24.346	25.786	−9.0	0.887	7.202
	7	−5.7	2.029	3.402	−8.7	0.485	4.843
	8	−5.4	2.106	3.475	−8.5	1.318	6.758
	9	−5.4	24.398	26.768	−8.4	3.160	8.729
APX (1OAF)	1	−5.3	0.000	0.000	−7.9	0.000	0.000
	2	−5.1	2.216	4.794	−7.9	0.172	6.543
	3	−5.0	1.622	4.161	−7.7	0.304	7.685
	4	−5.0	3.064	4.934	−7.7	0.254	5.233
	5	−4.9	2.771	5.338	−7.6	1.547	7.508
	6	−4.9	1.941	4.777	−7.6	1.542	5.966
	7	−4.8	2.067	3.246	−7.4	1.426	5.795
	8	−4.8	1.925	4.785	−7.3	1.623	5.855
	9	−4.8	2.260	2.629	−7.0	2.103	7.881

radicals and reducing levels of hydrogen peroxide (HOO˙), a crucial element for alleviating cellular oxidative stress. The Ni-DAPH complex exhibits a stronger affinity for both enzymes, with lower binding energies, suggesting a more stable interaction.[62]

The binding affinities of DAPH and Ni–DAPH complex to CCP and APX were investigated *via* Auto Dock Vina.[63] The dock box used for this study covered a volume of 30 Å × 30 Å × 30 Å and 22 Å × 22 Å × 22 Å with a center at coordinates $x = -13$, $y = -1$, $z = 2$ and $x = 14$, $y = 62$, $z = 24$, for CCP (2X08) and APX (1OAF), respectively, enabling the active site of the enzymes to be targeted.

The docking results reveal that the Ni–DAPH complex has a higher binding affinity for both HEME-enzymes studied than the free ligand (DAPH). Indeed, the binding energies obtained for Ni–DAPH/CCP and Ni–DAPH/APX are −9.5 kcal mol⁻¹ and −7.9 kcal mol⁻¹, respectively, compared to less negative values observed for the interactions of the ligand alone with the same enzymes (Table 8). This energy difference indicates that the coordination of the ligand with the nickel atom strengthens the enzyme–ligand interactions, particularly with the CCP.

Furthermore, the inhibition constant (Ki) of the complex, measured at 1.060 μm for 2X08 and 1.584 μm for 1OAF, reinforces the hypothesis of its potential efficacy as an antioxidant agent.

$$Ki = e^{\Delta G/RT}$$

where,

$$R = 1.985 \times 10^{-3} \frac{\text{kcal}}{\text{mol K}} \text{ and } T = 298 \text{ K}$$

A ligand with a low inhibition constant (Ki) and a very negative affinity (ΔG) requires low concentrations to achieve the desired effect. This reduces the risk of side effects and improves therapeutic efficacy. Conversely, a high Ki indicates that high drug doses would be required, which could lead to toxicity or clinical inefficacy.

Discovery Studio software (Version 2016; BIOVIA, Dassault Systèmes, San Diego, 2016) was used to analyze and visualize the intermolecular interactions between the ligand, its nickel-
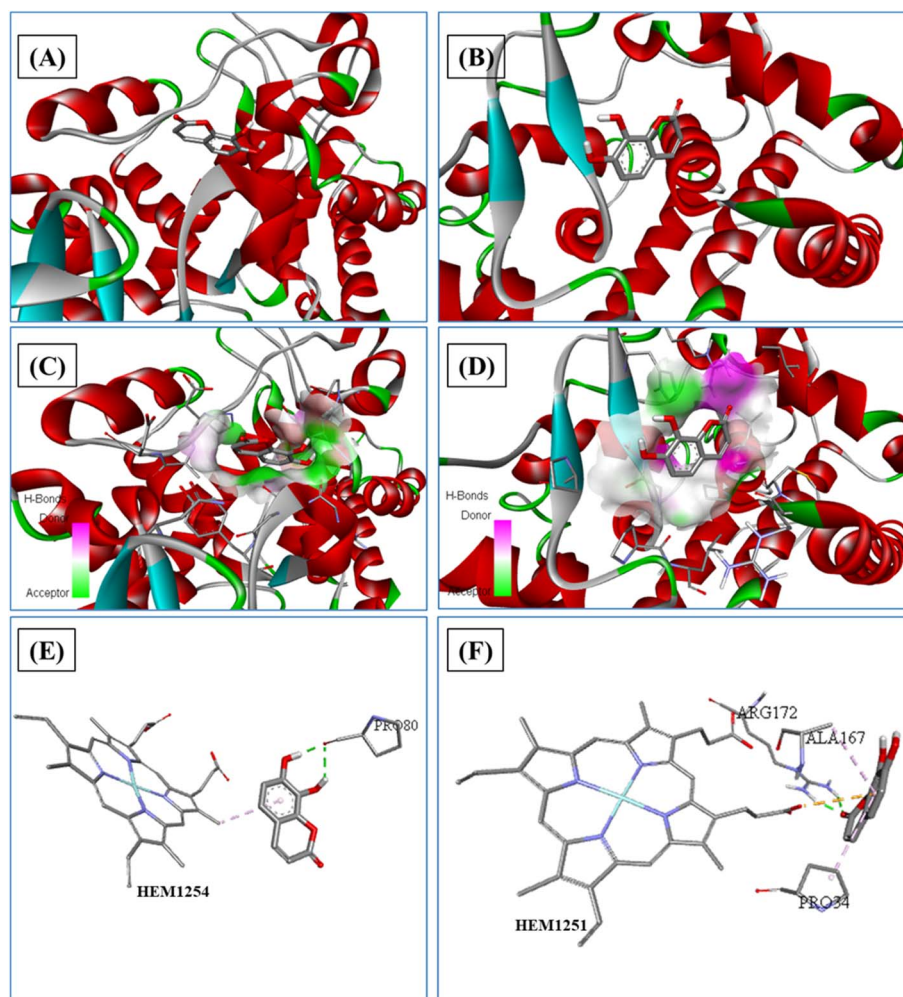

Fig. 11 3D detailed pose and binding mode of DAPH into catalytic active site of the receptors: (A) ribbon structure of receptor/2X08 protein, (B) ribbon structure of receptor/1OAF protein, (C) H-bonds (receptor/2X08 protein), (D) H-bonds (receptor/1OAF protein), (E) 3D form intermolecular interactions (receptor/2X08 protein), (F) 3D form intermolecular interactions (receptor/1OAF protein).

© 2025 The Author(s). Published by the Royal Society of Chemistry

based complex (Ni–DAPH), and the receptors targeted in the docking study. The interactions observed are illustrated in 3D and 2D in Fig. 11–13, providing a better understanding of the spatial arrangement of the bonds formed. Tables S7 and S8 summarize the types of interactions (hydrogen bonds, hydrophobic interactions, *etc.*) formed between the ligand or complex and the active residues of the receptors (2X08 and 1OAF).

In the Ni–DAPH -2X08 complex, eight conventional hydrogen interactions were observed, illustrating the importance of these bonds in stabilizing the complex. Among these, a hydrogen bond is formed between residue SER81 and the O atom of the ligand, with a distance measured at 2.896 Å, testifying to a strong interaction. Another significant three bonds are observed between the H atoms of the ligand and residue ARG184, with a distance of 2.061, 2.075 and 2.352 Å. In addition, residue ASP79 establishes a hydrogen bond with the H atom of the ligand, measured at 1.816 Å. Other important interactions include those between ARG184 and the H atom (2.352 Å), LEU182 and the H atom (2.374 Å) and GLY186 and the

O atom (3.221 Å). These interactions form a major part of the stabilizing interactions in this complex Ni–DAPH-2X08, reinforcing the affinity between ligand and receptor.

In the Ni–DAPH-1OAF complex, a similar set of eight hydrogen interactions was identified, also demonstrating their essential role in the stability of this system. A significant hydrogen bond is formed between residue ARG172 and the O atom of the ligand, with a distance of 2.922 Å. Residue ALA168 interacts with the H atom at a distance of 2.331 Å, while GLU176 forms a hydrogen bond with the H atom of the ligand at 2.970 Å. HIS76 also establishes a hydrogen bond with the O4 atom, measured at 2.314 Å, illustrating a strong interaction. Furthermore, HEM1251 interacts with two hydrogen atoms at a distance of 2.672 and 2336 Å. Residue HIS169 also contributes to these stabilizing interactions by establishing two hydrogen bonds with atoms H (2.583 Å) and O (3.704 Å). These hydrogen bonds significantly enhance the stability of the Ni–DAPH-1OAF complex and demonstrate the effectiveness of hydrogen interactions in this type of system.
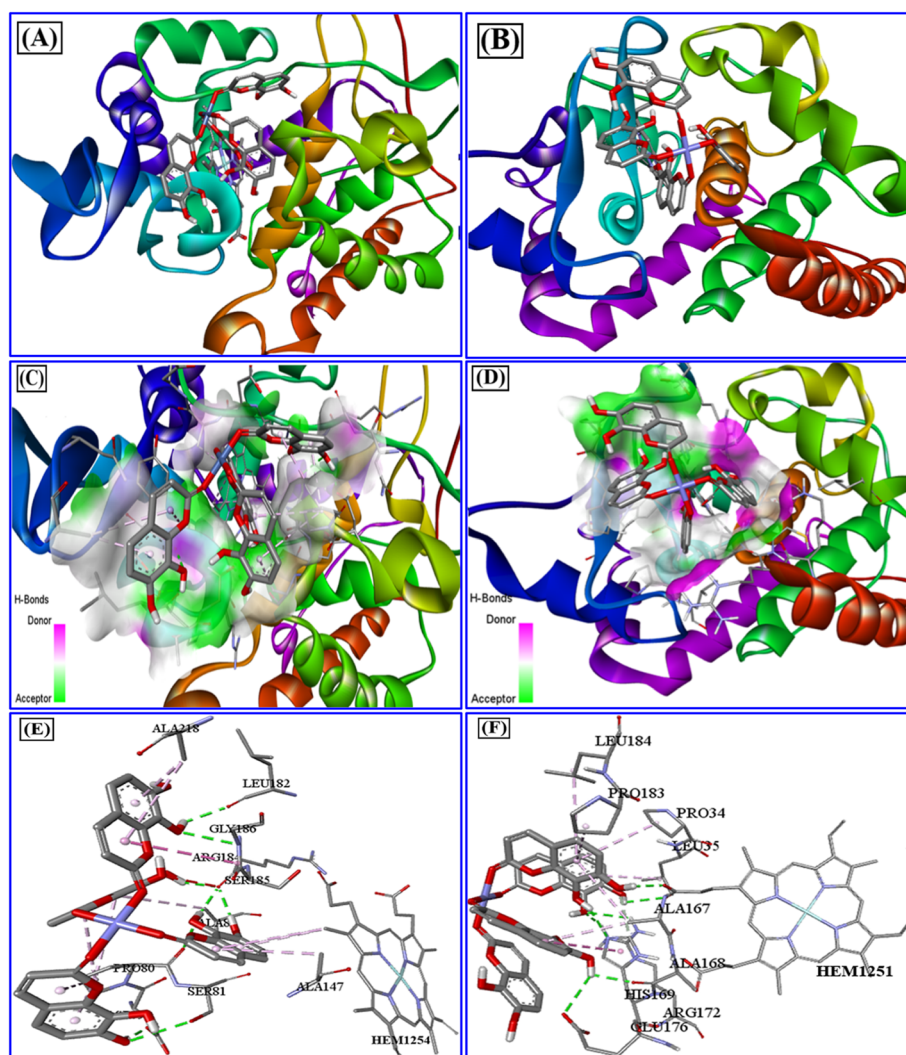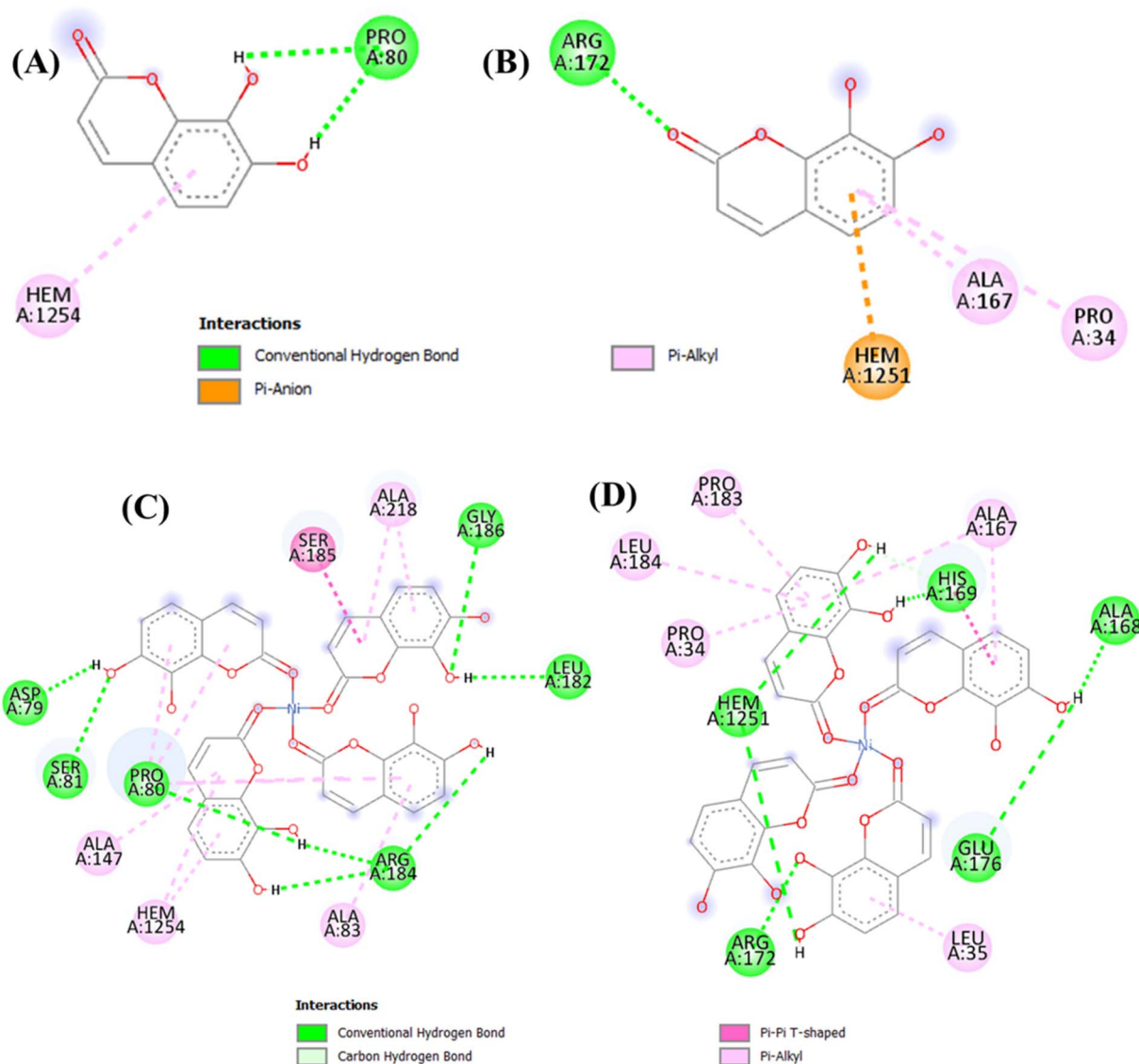

Fig. 12   3D detailed pose and binding mode of Ni–DAPH complex into catalytic active site of the receptors: (A) ribbon structure of receptor/2X08 protein, (B) ribbon structure of receptor/1OAF protein, (C) H-bonds (receptor/2X08 protein), (D) H-bonds (receptor/1OAF protein), (E) 3D form intermolecular interactions (receptor/2X08 protein), (F) 3D form intermolecular interactions (receptor/1OAF protein).

Fig. 13 2D receptor–ligand interaction diagram for (A) DAPH/2X08, (B) DAPH/1OAF, (C) Ni−DAPH complex/2X08 and (D) Ni−DAPH complex/1OAF.

In addition to hydrogen bonds, both complexes exhibit a variety of hydrophobic interactions. These include π–π T-shaped, alkyl and π-alkyl interactions, as illustrated in Fig. 11–13. Although generally weaker than hydrogen bonds, these hydrophobic interactions mainly involve the aromatic rings and alkyl chains of the ligand and protein residues, playing a complementary role in stabilizing the complexes. When docking with a HEME enzyme like CCP or APX, it is important to keep the HEME group (HEM1254 for CCP and HEM1251 for APX) as it is crucial for both catalytic activity and substrate interaction. Removing HEME can be used for exploratory studies, but limits information on physiologically relevant interactions. Retaining HEME reflects natural conditions and enhances the relevance of results particularly in oxidative or reducing properties.

Compared to the DAPH ligand, the Ni−DAPH complex establishes a greater number of interactions, both strong and weak, which indicates a higher affinity for enzyme receptors. The coordination of the ligand with the nickel atom appears to enhance the stability of the complex and intensify interactions with key residues of the enzyme active sites, which could explain the higher affinity observed compared to the free ligand.

These results reinforce the growing interest in nickel complexes and similar compounds, which demonstrate not only affinity for antioxidant enzymes such as CCP and APX, but also a stabilizing effect on HOO˙. However, while these results are promising, *in vitro* and *in vivo* biological studies are essential to confirm the therapeutic potential of our complex, particularly in the context of treatments targeting oxidant-associated pathologies.

4.13 ADMET study

The ADMET properties of DAPH and Ni−DAPH compounds were analyzed using the online platforms ADMETlab 2.0[64] for

Table 9 Predicted ADMET properties for the DAPH molecule and its Ni–DAPH metal complex using the ADMETlab 2.0 and Protox II platforms

Compounds	PPB[a] (%)	BBB[b]	HIA[c]	CL[d]	$T_{1/2}$[e]	LD₅₀[f] (mg kg⁻¹)	TPSA[g] (Å²)	NHD[h]	NHA[i]	NRB[j]	MW[k] (g mol⁻¹)	MLOGP[l]	Lipinski's violation
								Based on Lipinski rule					
DAPH	78.77	0.004	0.012	13.611	1.375	1540	70.67	2	4	0	178.03	0.772	0
Ni–DAPH	99.12	0.004	0.96	5.989	0.957	5370	247.87	8	16	4	776.09	4.071	3

[a] Plasma Protein Binding. [b] Blood–Brain Barrier Penetration. [c] Human Intestinal Absorption. [d] Plasma Clearance. [e] half-life drugs. [f] Lethal Dose. [g] Topological polar surface area. [h] Number of hydrogen bond donors. [i] Number of hydrogen bond acceptors. [j] Number of rotatable bonds. [k] Molecular weight. [l] calculated lipophilicity.

pharmacokinetic predictions and Protox II[65] for toxicity assessment (Table 9). This study revealed significant differences between the free molecule (DAPH) and its metal complex (Ni–DAPH). In terms of pharmacokinetics, the DAPH molecule has a moderate plasma protein binding (PPB) rate (78.77%), extremely low human intestinal absorption (HIA) (0.012) and relatively high plasma clearance (13.611 mL per min per kg), suggesting rapid elimination from the body. In contrast, the Ni–DAPH complex is characterized by very high intestinal absorption (0.96), a PPB close to 100% (99.12%) and lower clearance (5.989 mL per min per kg), indicating better potential bioavailability and longer retention in the body. Although the half-life of DAPH (1.375 h) is slightly longer than that of Ni–DAPH (0.957 h), both compounds show relatively short action. From a toxicological point of view, the Ni–DAPH complex has significantly lower acute toxicity (LD₅₀ = 5370 mg kg⁻¹) compared to DAPH (LD₅₀ = 1540 mg kg⁻¹), demonstrating a significant improvement in the safety of the compound after complexation.

Analysis of the physicochemical parameters also highlights marked differences. The DAPH molecule has a low molecular weight (178.03 g mol⁻¹) and a moderate topological polar surface area (TPSA) of 70.67 Å². It complies with all of Lipinski's rules, with 0 hydrogen bond donors and 4 hydrogen bond acceptors, no single rotatable bonds, and moderate lipophilicity (M log P = 0.772). These characteristics indicate good oral absorption potential according to conventional criteria. However, the Ni–DAPH complex has a very high molecular weight (776.09 g mol⁻¹), an extensive polar surface area (247.87 Å²), and 8 hydrogen bond donors and 16 hydrogen bond acceptors, far exceeding the thresholds of Lipinski's rule. It thus accumulates three violations (NHD, NHA, MW), which could theoretically limit its passive membrane diffusion. However, despite these violations, the complex exhibits remarkable intestinal absorption, suggesting that alternative mechanisms may compensate for these limitations.

5. Conclusion

To explore the formation and stability of a novel synthesized coordination complex involving nickel as the transition metal and daphnetin or 7,8-dihydroxycoumarin (DAPH) as the ligand, a theoretical investigation is conducted using the Gaussian 09 software and the TD-DFT calculation method.

The complex exhibits a tetradentate square planar structure, featuring four dative bonds formed between the nickel ion and the DAPH ligand, specifically at the Ni–C=O positions. This finding was validated through the vibrational frequencies of the NI–DAPH complex, revealing a significant elevation in the wavenumber associated with the carbonyl of the benzopyrone ring.

Analysis of the energies of the HOMO and LUMO frontier orbitals, atomic charges, and molecular electrostatic potentials of the Ni–DAPH complex facilitated the identification of nucleophilic sites, located at the oxygen atoms of the carbonyl groups, and the electrophilic site, situated at the nickel ion. Theoretical analysis played a crucial role in identifying the most stable structure among the four proposed structures of the Ni–DAPH complex.

The analysis of ¹H NMR chemical shifts in both the complex and the free ligand indicates that all protons, including those of the hydroxyl groups, have experienced a downfield shift. This shift signifies the active involvement of these protons in the metal–ligand interactions.

The second-order perturbation energies associated with Ni–O coordination suggest a more robust stabilization of the structure. NBO analysis reveals that all angles within the complex structure exhibit nearly identical values, indicative of symmetry. Moreover, the order of the 3d orbitals was determined to be dx2−y2 > dz2 > dxz > dyz > dxy.

The examination utilizing the QTAIM strongly supports the existence of ionic bonding with a discernible degree of covalency. Furthermore, an analysis of the ELF values for the Ni–DAPH complex indicates that pure ionic bonding has occurred in the interstitial region, away from the nuclei. Additionally, investigations employing the LOL suggest the existence of a region for delocalized electrons.

In conclusion, the complex formed between nickel and daphnetin exhibits significantly higher antioxidant potential compared to free daphnetin. This enhanced activity can be attributed to the coordination of the metal ion, which not only stabilizes reactive intermediates but also facilitates redox reactions that are crucial for effective free radical scavenging.

Molecular docking tools were employed to evaluate the antioxidant properties of the studied complexes, and the results indicated that these complexes could serve as potential inhibitors of cytochrome C peroxidase (CCP) and ascorbate peroxidase (APX) HEME-proteins. The promising antioxidant capacity of the [Ni–DAPH] complex opens new avenues for

pharmacological applications, particularly in the development of novel antioxidant agents for therapeutic use. The Ni–DAPH complex exhibits better ADMET properties than the DAPH molecule alone, despite some violations of Lipinski's rules. It is therefore a promising candidate for future biological applications.

Conflicts of interest

There are no conflicts to declare.

Data availability

The data supporting this article have been included as part of the SI. See DOI: https://doi.org/10.1039/d5ra03168k.

References

1 H. Henkea, W. Kandiollera, M. Hanif, B. K. Kepplera and C. G. Hartinger, Organometallic ruthenium and osmium compounds of pyidin-2-and-4-ones as potential anticancer agents, *Chem. Biodiversity*, 2012, **9**, 1718–1727, DOI: 10.1002/cbdv.20120.0005.

2 X. Zhang, L. Hu, X. Wang, Y. Zhao and X. Chen, Cu(II) and Zn(II) crystal complexes based on pyrazolone: Synthesis and application as antibacterial agents, *Inorg. Chim. Acta*, 2023, **556**, 121618, DOI: 10.1016/j.ica.2023.121618.

3 T. B. Boit, A. S. Bulger, J. E. Dander and N. K. Garg, Activation of C–O and C–N bonds using non-precious-metal catalysis, *ACS Catal.*, 2020, **10**, 12109–12126, DOI: 10.1021/acscatal.0c033.34.

4 J. Patel, H. Dholariya, K. Patel, J. Bhatt and K. Patel, Cu(II) and Ni(II) complexes of coumarin derivatives with fourth generation flouroquinolone: synthesis, characterization, microbicidal and antioxidant assay, *Med. Chem. Res.*, 2014, **23**, 3714–3724, DOI: 10.1007/s00044-014-0943-y.

5 B. M. Geetha, K. N. Brinda, G. Achar, J. G. Malecki, M. Alwarsamy, V. S. Betageri and S. Budagumpi, Coumarin incorporated 1,2,4–triazole derived silver(I) N–heterocyclic carbene complexes as efficient antioxidant and antihaemolytic agents, *J. Mol. Liq.*, 2020, **301**, 112352, DOI: 10.1016/j.molliq.2019.112352.

6 K. N. H. Rahman, J. Haribabu, C. Balachandran, N. S. P. Bhuvanesh, R. Karvembu and A. Sreekanth, Copper, nickel and zinc complexes of 3-acetyl coumarin thiosemicarbazone: Synthesis, characterization and *in vitro* evaluation of cytotoxicity and DNA/protein binding properties, *Polyhedron*, 2017, **135**, 26–35, DOI: 10.1016/j.poly.2017.06.044.

7 M. Grazula and E. Budzisz, Biological activity of metal ions complexes of chromones, coumarins and flavones, *Coord. Chem. Rev.*, 2009, **253**, 2588–2598, DOI: 10.1016/j.ccr.2009.06.015.

8 A. Carneiro, M. J. Matos, E. Uriarte and L. Santana, Trending Topics on Coumarin and Its Derivatives in 2020, *Molecules*, 2021, **26**, 501, DOI: 10.3390/molecules26020501.

9 U. Wang, W. Zhang, J. Dong and J. Gao, Design, synthesis, and bioactivity evaluation of coumarin-chalcone hybrids as potential anticancer agents, *Bioorg. Chem.*, 2020, **95**, 103530, DOI: 10.1016/j.biobrg.2019.103530.

10 A. Rawat, A.V.B. ReddyRecent advances on anticancer activity of coumarin derivatives, *Eur. J. Med. Chem.*, 2022, **5**, 100038, DOI: 10.1016/j.ejmcr.2022.100038.

11 O. S. Ipek, B. O. Sucu, S. Gul, C. Yolacan and M. Guzel, Synthesis of Novel Hybrid Lonidamine-Coumarin Derivatives and Their Anticancer Activities, *J. Mol. Struct.*, 2023, **1281**, 135114, DOI: 10.1016/j.molstruc.2023.135114.

12 X. Y. Sun, T. Liu, J. Sun and X. J. Wan, Synthesis and application of coumarin fluorescence probes, *RSC Adv.*, 2020, **10**, 10826–10847, DOI: 10.1039/c9ra10290f.

13 H. Raunio, O. Pentikaeinen and R. O. Juvonen, Coumarin-based profluorescent and fluorescent substrates for determining xenobiotic-metabolizing enzyme activities in vitro, *Int. J. Mol. Sci.*, 2020, **21**, 4708, DOI: 10.3390/ijms21134708.

14 A. Kumar, S. Jha and S. P. Pattanayak, Daphnetin ameliorates 7,12-dimethylbenz [a] anthracene-induced mammary carcinogenesis through Nrf-2-Keap1 and NF-κB pathways, *Biomed. Pharmacother.*, 2016, **82**, 439–448, DOI: 10.1016/j.biopha.2016.05.028.

15 P. Wróblewska-Łuczka, A. Góralczyk and J. J. Ł. Daphnetin, a Coumarin with Anticancer Potential against Human Melanoma: In Vitro Study of Its Effective Combination with Selected Cytostatic Drugs, *Cells*, 2023, **12**, 1593, DOI: 10.3390/cells12121593.

16 L. Zhang, Y. Gu, Z. Lina, G. Yue, C. Haiwei, C. Huixia, L. Bing, Z. Hong and S. Fengmin, Daphnetin protects against cisplatin-induced nephrotoxicity by inhibiting inflammatory and oxidative response, *Int. Immunopharmacol.*, 2018, **65**, 402–407, DOI: 10.1016/j.intimp.2018.10.018.

17 P. Aguirre, O. García-Beltrán, V. Tapia, Y. Muñoz, B. K. Cassels and M. T. Nunez, Neuroprotective effect of a new 7,8-dihydroxycoumarin-based Fe^{2+}/Cu^{2+} chelator in cell and animal models of Parkinson's disease, *ACS Chem. Neurosci.*, 2016, **8**, 178–185, DOI: 10.1021/acschemneuro.6b00309.

18 R. Vinayagam and B. Xu, 7, 8-Dihydroxycoumarin (Daphnetin) protects INS-1 pancreatic β-cells against streptozotocin-induced apoptosis, *Phytomedicine*, 2017, **24**, 119–126, DOI: 10.1016/j.phymed.2016.11.023.

19 Z. Wei, N. Wei, L. Su and S. Gao, The molecular effects underlying the pharmacological activities of daphnetin, *Front. Pharmacol*, 2024, **15**, 1–16, DOI: 10.3389/fphar.2024.1407010.

20 Ł. Balewski, S. Szulta, A. Jalińska and A. Kornicka, A Mini-Review: Recent Advances in Coumarin-Metal Complexes With Biological Properties, *Front. Chem.*, 2021, **9**, 781779, DOI: 10.3389/fchem.2021.781779.

21 D. Dehari, A. Jashari, S. Dehari and A. Shabani, New Complexes of Nickel (II) Using 4-Hydroxy-2-Oxo-2H-Chromene-3-Carboxamide as Ligand, *Int. J. Chem. Eng.*,

2012, **6**, 641–644. https://www.researchgate.net/publication/283091123.

22 M. J. Frisch, *et al. Gaussian 09, Revision B. 01*. Gaussian, Inc., Wallingford, 2009.

23 M. Macit, H. Tanak, M. Orbay and N. Özdemir, Synthesis, crystal structure, spectroscopic Characterization and DFT studies of bis [(1Z, 2E)-N-(2,6-diethylphenyl)-N'-hydroxy-2-(hydroxyimino) acetimidamidato] nickel (II), *Inorg. Chim. Acta*, 2017, **459**, 36–44, DOI: 10.1016/j.ica.2017.01.013.

24 M. Torrent, M. Sola and G. Frenking, Theoretical studies of some transition-metal-mediated reactions of industrial and synthetic importance, *Chem. Rev.*, 2000, **10**, 439–493, DOI: 10.1021/cr980452i.

25 M. S. Khaikin and N. F. Rakova, Ultraviolet spectra of some 6, 7- and 7, 8-dihydroxycoumarins, *J. Appl. Spectrosc.*, 1968, **8**, 640–642, DOI: 10.1007/BF00618390.

26 M. F. H. Al-Kadhemy, Z. S. Rasheed and S. R. Salim, Fourier transform infrared spectroscopy for irradiation coumarin doped polystyrene polymer films by alpha ray, *J. Radiat. Res. Appl. Sci.*, 2016, **9**, 321–331, DOI: 10.1016/j.jrras.2016.02.004.

27 J. R. Cheeseman, G. W. Trucks, T. A. Keith and M. J. Frisch, A comparison of models for calculating nuclear magnetic resonance shielding tensors, *J. Chem. Phys.*, 1996, **104**, 5497–5509, DOI: 10.1063/1.471789.

28 A. Irfan, A. G. Al-Sehemi, S. Muhammad, M. S. Al-Assiri, A. R. Chaudhry, A. Kalam and M. Shkir, Electro-optical and charge injection investigations of the donor-π-acceptor triphenylamine, oligocene–thiophene–pyrimidine and cyanoacetic acid based multifunctional dyes, *J. King Saud Univ., Sci.*, 2015, **316**, 113809, DOI: 10.1016/j.jksus.2015.06.002.

29 L. A. Cameron, J. W. Ziller and A. F. Heyduk, Near-IR absorbing donor–acceptor ligand-to-ligand charge-transfer complexes of nickel (II), *Chem. Sci.*, 2016, **7**, 1807–1814, DOI: 10.1039/c5sc02703a.

30 Y. Boulmokh, K. Belguidoum, F. Meddour and H. Amira-Guebailia, Investigation of antioxidant activity of epigallocatechin gallate and epicatechin as compared to resveratrol and ascorbic acid: experimental and theoretical insights, *Struct. Chem.*, 2021, **32**, 1907–1923, DOI: 10.1007/s11224-021-01763-5.

31 H. Chermette, Chemical reactivity indexes in density functional theory, *J. Comput. Chem.*, 1999, **20**, 129–154, DOI: 10.1002/(SICI)1096-987X(19990115)20:1<129::AID-JCC13>3.0.CO;2-A.

32 P. Atkins and J. Paula. *Physical Chemistry*. OUP Oxford, 2010.

33 C. B. Hubschle and S. V. Smaalen, The electrostatic potential of dynamic charge densities, *J. Appl. Crystallogr.*, 2017, **50**, 1627–1636, DOI: 10.1107/S1600576717013802.

34 E. D. Glendening, D. M. Hiatt and F. Weinhol. Natural Bond Orbital Analysis of Chemical Structure, Spectroscopy, and Reactivity: How it Works. *Comprehensive Computational Chemistry*, 2023, 2, pp 406–421 doi: DOI: 10.1016/B978-0-12-821978-2.00077-5.

35 M. Kurt, P. Chinna Babu, N. Sundaraganesan, M. Cinar and M. Karabacak, Molecular structure, vibrational, UV and NBO analysis of 4-chloro-7-nitrobenzofurazan by DFT calculations, *Spectrochim. Acta, Part A*, 2011, **7**, 1162–1170, DOI: 10.1016/j.saa.2011.04.037.

36 W. R. Mason and H. B. Gray, Electronic structures of square planar complexes, *J. Am. Chem. Soc.*, 1968, **90**, 5721–5729, DOI: 10.1021/JA010.23A012.

37 A. Takashiro, K. Seiko and U. Akio, Assignment of d-d transitions of square planar [CuIIN4] complexes containing imidate and amine ligands by means of polarized crystal spectra, *Bull. Chem. Soc. Jpn.*, 2001, **74**, 851–860, DOI: 10.1246/bcsj.74.851.

38 J. Borgel, M. G. Campbell and T. Ritter, Transition metal d-orbital splitting diagrams: an updated educational resource for square planar transition metal complexes, *J. Chem. Educ.*, 2016, **93**, 118–121, DOI: 10.1021/acs.jchem.ed.5b005.42.

39 C. Banciu and C. I. Lepadatu, Electronic transitions in square planar complexes with Ni (d8)-N(sp2) bonds, *Z. Physiol. Chem.*, 1975, **97**, 197–205, DOI: 10.1524/zpch.1975.97.3_4.197.

40 A. Midoune and A. Messaoudi, DFT/TDDFT studies of the structural, electronic and NBO properties of some complexes with the tetrathiafulvalene-1, 3-benzothiazole ligand, *Inorg. Chim. Acta*, 2021, **516**, 120151, DOI: 10.1016/j.ica.2020.120151.

41 V. Balachandran, T. Karthick, S. Perumal and A. Nataraj, Comparative theoretical studies on natural atomic orbitals, natural bond orbitals and simulated UV-visible spectra of N-(methyl) phthalimide and N-(2 bromoethyl) phthalimide, *Indian J. Pure Appl. Phys.*, 2013, **51**, 178–184 http://nopr.niscpr.res.in/handle/123456789/16074.

42 V. Nivetha, V. Ragavendran, V. Santhanam, B. Logeswaran and S. Kaleeswaran, Experimental and computational insights into the synthesis and characterization of a novel Schiff base ligand 2, 20-[(1z, 14e)-2, 5, 8,11,14-pentaazapentadeca-1, 14-diene-diyl] diphenol, *CSIT*, 2021, **91**, 71–81, DOI: 10.1007/s40012-020-00322-3.

43 R. F. W. Bader and C. F. Matta, Bonding to titanium, *Inorg. Chem.*, 2001, **40**, 5603–5611, DOI: 10.1021/ic010165o.

44 D. Cremer and E. Kraka, Chemical bonds without bonding electron density—does the difference electron-density analysis suffice for a description of the chemical bond, *Angew Chem. Int. Ed. Engl.*, 1984, **23**, 627–628, DOI: 10.1002/anie.198406271.

45 P. Jerabek, B. Von Der Esch, H. Schmidbaur and P. Schwerdtfeger, Influence of Relativistic Effects on Bonding Modes in M (II) Dinuclear Complexes (M = Au, Ag, and Cu), *Inorg. Chem.*, 2017, **56**, 14624–14631, DOI: 10.1021/acs.inorgchem.7b02434.

46 X. Li, S. Huo, Y. Zeng, Z. Sun, S. Zheng and L. Meng, Metal–Metal and Metal–Ligand Bonds in (η^5-C_5H_5) 2M2 (M = Be, Mg, Ca, Ni, Cu, Zn), *Organometallics*, 2013, **32**, 1060–1066, DOI: 10.1021/om301110j.

47 A. D. Becke and K. E. Edgecombe, A simple measure of electron localization in atomic and molecular systems, *J. Chem. Phys.*, 1990, **92**, 5397–5403, DOI: 10.1063/1.458517.

48 Y. Boulmokh, K. Belguidoum, F. Meddour and H. Amira-Guebailia, Enhanced Antioxidant Properties of Novel Curcumin Derivatives: A Comprehensive DFT Computational Study, *Struct. Chem.*, 2024, **35**, 825–839, DOI: **10.21203/rs.3.rs-3258839/v1**.

49 A. Benayahoum, H. Amira-Guebailia and O. Houache, A DFT method for the study of the antioxidant action mechanism of resveratrol derivatives, *J. Mol. Model.*, 2013, **19**, 2285–2298, DOI: **10.1007/s00894-013-1770-7**.

50 J. Rimarcík, V. Lukeš, E. Klein and M. Ilcin, Study of the solvent effect on the enthalpies of homolytic and heterolytic N–H bond cleavage in p-phenylenediamine and tetracyano-p-phenylenediamine, *Theochem*, 2010, **952**, 25–30, DOI: **10.1016/j.theochem.2010.04.002**.

51 J. Sushmitha, R. Sruthi, K. Aishwarya, M. Sivasubramanian, S. Priyadharshini and S. Stalin, Transition Metal Coordination Complexes of Flavonoids: A Class of Better Pharmacological Active Molecules to Develop New Drugs, *Adv. Anticancer Agents Med. Chem.*, 2023, **23**, 417–431, DOI: **10.2174/1871520622666220520093018**.

52 M. H. M. Belhachemi, A. Benmohammed, H. Saiah, N. Boukabcha, M. Saidj, N. Dege, A. Djafri and A. Chouaih, Synthesis, structural determination, molecular docking and biological activity of 1-(4-fluorobenzyl)-5-bromolindolin-2,3-dione, *J. Mol. Struct.*, 2022, **1265**, 133342, DOI: **10.1016/j.molstruc.2022.133342**.

53 A. R. Guerroudj, N. Boukabcha, A. Benmohammed, N. Dege, N. E. H. Belkafouf, N. Khelloul, A. Djafri and A. Chouaih, Synthesis, crystal structure, vibrational spectral investigation, intermolecular interactions, chemical reactivity, NLO properties and molecular docking analysis on (E)-N-(4-nitrobenzylidene)-3-chlorobenzenamine: A combined experimental and theoretical study, *J. Mol. Struct.*, 2021, **1240**, 130589, DOI: **10.1016/j.molstruc.2021.130589**.

54 F. Z. Boudjenane, Z. D. Benyahlou, M. H. M. Belhachemi, N. Boukabcha, Ö. Tamer, S. Yahiaoui, Y. Atalay, E. Tarcan and A. Chouaih, A theoretical investigation on Hirshfeld surface, IR., UV–Vis, 1H and 13C NMR spectra, nonlinear optical properties, and in silico molecular docking of an organometallic compound: Dibromobis (l-proline)zinc(II), *Comput. Theor. Chem.*, 2023, **1229**, 114345, DOI: **10.1016/j.comptc.2023.114345**.

55 B. Smail, A. Bouchama, R. Rahmani, A. Djafri, Z. D. Benyahlou, N. Taibi, N. Dege, M. H. M. Belhachemi, K. Bachari and A. Chouaih, Slow evaporation synthesis, crystal structure, DFT calculations, molecular docking, and pharmacokinetic studies of hexaaquazinc(II) dihydrogen benzene-1,2,4,5-tetracarboxylate, *J. Coord. Chem.*, 2024, **77**, 543–562, DOI: **10.1080/00958972.2024.2332895**.

56 A. Chebli, A. Djafri, N. Boukabcha, Y. Megrouss, M. Drissi, M. H. M. Belhachemi, S. Yahiaoui, A. R. Guerroudj, A. Chouaih and A. Djafri, Synthesis, crystal structure, DFT calculations, NBO, Fukui function, NCI-RDG, Hirshfeld surface analysis, NLO properties and molecular docking analysis on (E)-N'-(3-methoxybenzylidene)-2-(quinolin-8-yloxy) acetohydrazide, *J. Mol. Struct.*, 2024, **1310**, 138287, DOI: **10.1016/j.molstruc.2024.138287**.

57 E. J. Murphy, C. L. Metcalfe, J. Basran, P. C. E. Moody and E. L. Raven, Engineering the Substrate Specificity and Reactivity of a Heme Protein: Creation of an Ascorbate Binding Site in Cytochrome c Peroxidase, *Biochem*, 2008, **47**, 13933–13941, DOI: **10.1021/bi801480r**.

58 K. H. Sharp, M. Mewies, P. C. E. Moody and E. L. Raven, Crystal structure of the ascorbate peroxidase–ascorbate complex, *Nat. Struct. Mol. Biol.*, 2003, **10**, 303–307, DOI: **10.1038/nsb913**.

59 RCSB PDB: Homepage, **https://www.rcsb.org/**, accessed 01 October 2024.

60 H. Wu, H. Peng, Y. Zhang, F. Wang, H. Zhang, C. Wang and Z. Yang, Synthesis, crystal structure, electrochemistry and antioxidative activity of copper(II), manganese(II) and nickel(II) complexes containing bis(N-ethylbenzimidazol-2-ylmethyl)aniline, *Appl. Organomet. Chem.*, 2015, **29**, 443–449, DOI: **10.1002/aoc.3313**.

61 Y. Wang, Z. Yang and B. W. Synthesis, Characterization and Anti-oxidative Activity of Cobalt (II), Nickel(II) and Iron(II) Schiff Base Complexes, *Transition Met. Chem.*, 2005, **30**, 879–883, DOI: **10.1007/s11243-005-6166-9**.

62 Y. T. Meharenna, P. Oertel, B. Bhaskar and T. L. Poulos, Engineering Ascorbate Peroxidase Activity into Cytochrome c-Peroxidase, *Biochem*, 2008, **47**, 10324–10332, DOI: **10.1021/bi8007565**.

63 A. Allouche, Gabedit — A Graphical User Interface for Computational Chemistry Softwares, *J. Comput. Chem.*, 2012, **32**, 174–182, DOI: **10.1002/jcc.21600**.

64 G. Xiong, Z. Wu, J. Yi, L. Fu, Z. Yang, C. Hsieh, M. Yin, X. Zeng, C. Wu, A. Lu and X. Chen, ADMETlab 2.0: an integrated online platform for accurate and comprehensive predictions of ADMET properties, *Nucleic Acids Res.*, 2021, **49**, W5–W14, DOI: **10.1093/nar/gkab255**.

65 P. Banerjee, A. O. Eckert, A. K. Schrey and R. Preissner, ProTox-II: a webserver for the prediction of toxicity of chemicals, *Nucleic Acids Res.*, 2018, **46**, W257–W263, DOI: **10.1093/nar/gky318**.

© 2025 The Author(s). Published by the Royal Society of Chemistry